Icarus 227 (2014) 152–175

Contents lists available at ScienceDirect

Icarus

journal homepage: www.elsevier.com/locate/icarus

Noncircular features in Saturn's rings I: The edge of the B ring

Philip D. Nicholson [a,*], Richard G. French [b], Matthew M. Hedman [c], Essam A. Marouf [d], Joshua E. Colwell [e]

[a] Department of Astronomy, Cornell University, Ithaca, NY 14853, United States
[b] Department of Astronomy, Wellesley College, Wellesley, MA 02481, United States
[c] Department of Physics, University of Idaho, Moscow, ID 83844, United States
[d] Department of Electrical Engineering, San Jose State University, San Jose, CA 95192, United States
[e] Department of Physics, University of Central Florida, Orlando, FL 32816, United States

ARTICLE INFO

Article history:
Received 26 May 2013
Revised 1 September 2013
Accepted 1 September 2013
Available online 21 September 2013

Keywords:
Occultations
Planetary rings
Saturn, rings

ABSTRACT

A comprehensive investigation of all available radio and stellar occultation data for the outer edge of Saturn's B ring, spanning the period 1980–2010, confirms that the $m = 2$ distortion due to the strong Mimas 2:1 inner Lindblad resonance circulates slowly relative to Mimas in a prograde direction, with a frequency $\Omega_L = 0.1819^\circ\ \mathrm{d}^{-1}$. Our best-fitting model implies that the radial amplitude of this distortion ranges from a minimum of 3 km to a maximum of 71 km, with short-lived minima recurring every 5.42 yrs. In addition to the dominant $m = 2$ pattern, the edge of the B ring also exhibits at least four other perturbations. An $m = 1$ component with a radial amplitude of ~20 km rotates at a rate very close to the expected local apsidal precession rate of $\varpi_B \sim 5.059^\circ\ \mathrm{d}^{-1}$, while smaller perturbations are seen with $m = 3$ (amplitude 12.5 km), $m = 4$ (5.9 km), and $m = 5$ (5.6 km), each of which has a pattern speed consistent with that expected for a spontaneously-generated "normal mode" (French, R.G. et al. [1988]. Icarus 73, 349–378). Our results for $m = 1$, $m = 2$ and $m = 3$ are compatible with those obtained by Spitale and Porco (Spitale, J.N., Porco, C.C. [2010]. Astron. J. 140, 1747–1757), which were based on *Cassini* imaging data. The pattern speed of each normal mode slightly exceeds that expected at the mean edge radius, supporting their conclusion that they may represent a series of free modes, each of which is trapped in a narrow region between the mode's resonant radius and the ring's edge. However, both our model and that of Spitale and Porco fail to provide complete descriptions of this surprisingly complex feature, with post-fit root-mean-square residuals of ~8 km considerably exceeding typical measurement errors of 1 km or less.

1. Introduction

The sharp outer edge of Saturn's B ring, located at a radius of ~ 117,570 km, has long been associated with the 2:1 orbital resonance with the satellite Mimas. More specifically, Goldreich and Tremaine (1978) proposed that the 2:1 Inner Lindblad resonance (henceforth ILR) defines the location of this edge, and that the gravitational torque between Mimas and the perturbed ring material close to the edge balances the viscous transfer of angular momentum outwards through the B ring, thus preventing the B ring from spreading outwards. As a consequence of the resonant perturbations, the shape of the ring edge was expected to take the form of a two-lobed figure, rotating at the same angular velocity as Mimas. Algebraically, this may be expressed as

$$r(\lambda, t) \approx a - A\cos[2(\lambda - \lambda_M) - \phi], \qquad (1)$$

where r and λ are the local radius and longitude of the ring edge at time t, λ_M is the mean longitude of Mimas at this time and ϕ is a constant. This simple but elegant picture was apparently confirmed by *Voyager* observations, which revealed the expected two-lobed pattern of radial distortions on the edge, with an amplitude of $A \sim 75$ km and one radial minimum aligned with Mimas (i.e., $\phi \simeq 0$) (Porco et al., 1984). The B ring edge is the most noncircular feature in Saturn's rings, with the exception of the eccentric F ring (Bosh et al., 2002), and has since become the type-example of a resonantly-perturbed ring edge. We note, however, that this model was based on very few data: a radio occultation by the *Voyager 1* RSS experiment (Tyler et al., 1983), a stellar occultation by the *Voyager 2* PPS experiment (Lane et al., 1982; Esposito et al., 1983) and a mere half-dozen images with resolutions of 5–10 km/pixel (Porco et al., 1984).

Since the *Voyager* flybys in 1980/1981, and prior to the arrival of *Cassini* at Saturn in 2004, there have been relatively few additional observations of Saturn's rings with a spatial resolution sufficient to measure such radial distortions. In July 1989, an occultation of the bright star 28 Sgr was widely observed from telescopes in North

---

[*] Corresponding author.
E-mail address: nicholso@astro.cornell.edu (P.D. Nicholson).

http://dx.doi.org/10.1016/j.icarus.2013.09.002

and South America, yielding multiple high-quality optical depth profiles (Hubbard et al., 1993; French et al., 1993; Nicholson et al., 2000). With the advent of the Hubble Space Telescope (HST), occultations of fainter stars became feasible, and such observations were successfully made in 1991 (Elliot et al., 1993) and 1995 (Bosh et al., 2002). The question of the B ring edge's shape was again addressed by Bosh (1994), using data from both the 28 Sgr and the 1991 HST occultations as well as the two *Voyager* occultation points, who confirmed the two-lobed distortion locked to Mimas, but found a much smaller amplitude of $A \sim 23$ km.

With the advent of a wealth of new observations from the *Cassini* spacecraft, this simple picture has become rather more complex. Based on several high-resolution imaging sequences of the Cassini Division obtained in 2005, Spitale and Porco (2006) reported that the orientation of the 2-lobed pattern at the B ring's edge had changed, with one radial minimum being located $\sim 28°$ ahead of Mimas' longitude. Furthermore, the densely-sampled imaging data showed that additional perturbations, beyond the expected $m = 2$ distortion, were clearly present. In particular, they found evidence for an $m = 3$ perturbation, which has no obvious resonant explanation.

Using data from ~40 stellar occultations observed by the Visual and Infrared Mapping Spectrometer (VIMS) instrument on *Cassini*, together with data from 12 radio occultations by the Radio Science Subsystem (RSS), Hedman et al. (2010a) found that no simple $m = 2$ model, with a fixed orientation relative to Mimas, could fit all of the observations. In mid-2005, the best-fitting $m = 2$ pattern was found to lead Mimas by $\sim 35°$ in longitude (i.e., $\phi \simeq +70°$), with an amplitude of ~49 km, while in 2008 the pattern was found to lag Mimas by $\sim 20°$ (i.e., $\phi \simeq -40°$), but with a much greater amplitude of ~75 km. It thus appeared that between 2005 and 2008 the orientation of the $m = 2$ pattern had drifted *backwards* relative to Mimas, at a mean rate of $\sim 0.045°\ \mathrm{d}^{-1}$.

While consistent with the available occultation observations, such a steady drift seemed unlikely on physical grounds, and Hedman et al. (2010a) instead proposed a model in which the orientation of the $m = 2$ pattern oscillates, or *librates*, about the direction towards Mimas.[1] Augmenting the three years of available *Cassini* VIMS and RSS occultation data with the very limited set of *Voyager* and Earth-based occultation data stretching back to 1980, Hedman et al. (2010a) obtained least-squares fits that suggested possible angular libration frequencies of $\Omega_L = 0.058°\ \mathrm{d}^{-1}$ or $0.117°\ \mathrm{d}^{-1}$, corresponding to libration periods of 17.0 or 8.4 yrs, respectively. These simple models did not, however, take into account the amplitude variations expected to accompany any libration of ϕ.

An important clue was provided by an independent series of stellar occultations observed by the *Cassini* Ultraviolet Imaging Spectrometer instrument (UVIS), which showed that the amplitude of the radial distortion at the B ring edge had almost vanished in 2006/2007 (Esposito et al., 2009), a period when there were few VIMS or RSS occultations.

In the meantime, Spitale and Porco (2010) had analyzed an extensive set of high-resolution *Cassini* imaging observations of the B ring edge obtained between 2005 and 2009. With these data, they could estimate the amplitude and phase of the $m = 2$ perturbation from each azimuthal scan or ansa movie, finding systematic variations in both quantities. The amplitude was confirmed to have reached a minimum of only a few km in early 2007, but the phase angle ϕ appeared to have increased monotonically with time, rather than exhibiting the oscillation predicted by Hedman et al. (2010a). In order to appreciate this distinction, it is useful to examine the variations in A (usually expressed in terms of the dimensionless "eccentricity" $e_2 = A/a$) and ϕ expected for a test particle subject to perturbations by a nearby ILR. For a ring particle located interior to the ILR, these are illustrated in Fig. 1, adapted from Fig. 4 of Spitale and Porco (2010). The vector defined by the Cartesian components $[h = e\cos\phi, k = e\sin\phi]$ moves at a constant angular rate on a circle of radius e_f about a fixed point on the abscissa at $h = e_0$.

From this diagram, we see that there are two distinct possibilities. If e_f (known as the "free eccentricity") is less than e_0 (the "forced eccentricity"), then the phase angle librates about $\phi = 0$, as originally suggested by Hedman et al. (2010a). If $e_f > e_0$, on the other hand, then the phase angle circulates continuously through 2π radians. In both cases, the overall eccentricity, e_2 oscillates between a minimum of $|e_f - e_0|$ and a maximum of $e_f + e_0$. Based on the imaging data, Spitale and Porco (2010) concluded that ϕ circulates in a prograde direction, having increased monotonically from $\sim 70°$ in 2005, through 180° in 2007 (when the amplitude was at a minimum), to $\sim 320°$ in 2009. But the very small radial amplitude observed in both the imaging and UVIS data in late 2006 and early 2007 implies that the forced and free eccentricities are almost equal, which in turn means that choosing between a librating and circulating model is not easy.

Rather than explicitly using a variable amplitude and phase, Spitale and Porco (2010) chose to model the observed behavior directly in terms of a forced $m = 2$ perturbation of constant amplitude ae_0 locked to Mimas and thus rotating with the satellite's mean motion, n_M (which is the model originally proposed by Porco et al. (1984)), plus an $m = 2$ "normal mode" of amplitude ae_f rotating at a slightly faster angular rate, Ω_2. Mathematically, this prescription is equivalent to the geometric model illustrated in Fig. 1, with $\Omega_L = 2(\Omega_2 - n_M)$. Spitale and Porco (2010) found radial amplitudes for the forced and free modes of 34.6 km and 37.3 km, respectively, and their best-fitting value for the circulation frequency was $\Omega_L = 0.179 \pm 0.007°\ \mathrm{d}^{-1}$, corresponding to a counter-clockwise circulation of ϕ with a period of ~5.4 yrs.

After subtracting the dominant $m = 2$ perturbations, Spitale and Porco (2010) also found convincing evidence for $m = 1$ and $m = 3$ perturbations, with radial amplitudes of ~21 km and 12 km, respectively. Hedman et al. (2010a) had also found evidence for an $m = 1$ perturbation in the occultation data, with an amplitude of ~17 km and rotating at the apsidal precession rate expected for a Keplerian ellipse. Since these distortions are not directly attributable to the Mimas resonance, they are probably best thought of as free, or "normal" modes. Such modes were first

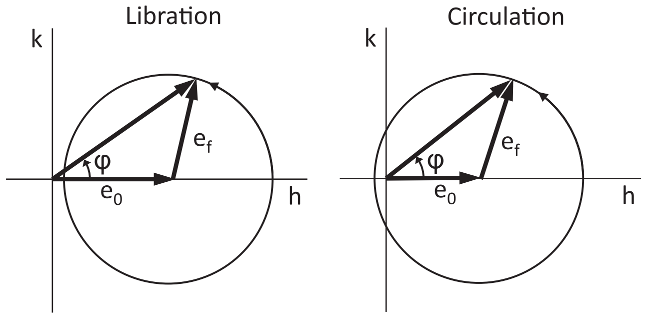

Fig. 1. A sketch of the possible librating and circulating models for the $m = 2$ perturbation at the edge of the B ring in terms of the resonant argument ϕ and overall amplitude $A = ae_2$, based on Eqs. (5) and (6) below. The forced and free eccentricities are e_0 and e_f, respectively. The diagram is drawn for an orbit interior to the resonant radius, so that the system librates (or circulates) in a counter-clockwise direction about a fixed point at $e = e_0$, $\varphi_0 = 0$. For an orbit exterior to the resonant radius, the situation is similar but the motion is clockwise about a fixed point at $\varphi_0 = \pi$.

---

[1] Mathematically, libration implies that the angle ϕ in Eq. (1) oscillates with a specified amplitude and angular frequency, Ω_L.

Table 1
B ring occultation data.

Event	Time (UTC at Saturn)	λ (°)	$(\lambda - \lambda_M)$[a] (°)	$(r - a)$[b] (km)	Resid.[c] (km)
VGR1 RSS	1980 NOV 13 03:29:45.26	96.72	18.72	−40.96	−9.94
VGR2 DelSco	1981 AUG 26 01:11:21.71	40.31	186.35	−66.92	−0.56
28 Sgr MCD-I	1989 JUL 03 05:00:38.11	32.30	27.18	−47.31	−0.33
28 Sgr PAL-I	1989 JUL 03 05:01:25.07	32.46	27.13	−48.52	−1.59
28 Sgr ESO1-I	1989 JUL 03 05:03:50.67	25.70	19.73	−39.09	7.03
28 Sgr ESO2-I	1989 JUL 03 05:03:50.71	25.70	19.73	−40.75	5.38
28 Sgr MCD-E	1989 JUL 03 07:55:00.53	222.99	171.61	−36.41	−4.02
28 Sgr PAL-E	1989 JUL 03 07:55:40.73	222.47	170.92	−35.15	−3.64
28 Sgr ESO1-E	1989 JUL 03 07:56:17.35	230.34	178.62	−60.55	−19.72
28 Sgr IRTF-E	1989 JUL 03 07:59:01.86	223.09	170.64	−33.73	−2.26
HST1081 HST-I	1991 OCT 03 05:54:58.68	247.65	148.99	−60.78	−11.96
HST1081 HST-E	1991 OCT 03 07:10:19.68	240.84	122.19	−21.32	−14.89
HST5824 HST-I	1995 NOV 21 06:03:15.69	253.41	65.34	−9.75	10.63
RSS 007I X14	2005 MAY 03 03:27:08.16	259.34	197.94	−77.06	−17.61
RSS 007E X43	2005 MAY 03 08:09:42.67	60.32	283.97	77.17	12.72
RSS 008I X43	2005 MAY 21 07:52:14.25	257.84	90.50	9.97	−1.40
RSS 008E X63	2005 MAY 21 12:38:53.05	62.23	178.86	−5.25	6.48
UVIS AlpLeo009I	2005 JUN 08 05:42:34.99	328.58	159.99	−56.99	−20.84
UVIS AlpLeo009E	2005 JUN 08 06:20:39.18	300.41	121.72	44.80	2.97
RSS 009E X14	2005 JUN 08 17:25:40.18	64.27	69.18	−10.18	−9.45
RSS 010I X14	2005 JUN 26 17:52:17.74	253.56	215.72	−40.14	−3.16
RSS 010E X14	2005 JUN 26 22:48:37.50	67.13	310.68	29.96	0.50
UVIS SigSgr011I	2005 JUL 14 23:34:44.26	276.32	111.92	42.83	0.66
RSS 011E X43	2005 JUL 15 05:34:49.48	70.69	170.77	5.61	12.92
RSS 012I X63	2005 AUG 02 08:26:39.17	247.45	266.20	−11.29	−6.38
RSS 012E X14	2005 AUG 02 13:30:35.45	74.70	12.83	−26.30	−0.53
VIMS alpSco013I	2005 AUG 20 11:49:04.89	290.98	220.26	−49.42	−0.84
VIMS alpSco013E	2005 AUG 20 13:41:43.58	355.68	255.07	−25.66	2.84
RSS 013E X14	2005 AUG 20 19:14:33.91	79.57	250.67	−0.95	−1.70
RSS 014I X14	2005 SEP 05 13:29:51.51	269.35	180.08	11.52	4.38
VIMS alpOri026I	2006 JUL 23 16:48:49.94	356.84	358.06	10.67	0.50
VIMS alpSco029I	2006 SEP 26 07:45:52.34	193.33	349.86	−39.93	−21.25
UVIS LamSco029E	2006 SEP 27 01:34:05.91	349.10	222.27	−20.03	−9.94
UVIS AlpAra032I	2006 NOV 09 21:22:49.87	221.12	273.56	30.76	11.49
UVIS AlpAra033I	2006 NOV 21 20:23:23.30	220.83	25.19	−24.14	−4.79
VIMS alpAur034I	2006 DEC 02 12:55:45.12	26.47	67.71	6.30	−3.83
UVIS AlpVir034I	2006 DEC 03 02:19:56.49	198.85	26.77	−16.23	4.74
UVIS AlpVir034E	2006 DEC 03 03:51:22.06	97.20	260.86	9.44	10.63
UVIS EtaLup034I	2006 DEC 03 11:38:13.35	171.70	211.52	8.42	12.05
UVIS EtaLup034E	2006 DEC 03 15:10:30.18	121.34	104.85	−16.59	−16.83
UVIS KapCen035E	2006 DEC 16 23:40:40.48	12.17	294.50	−19.22	−2.00
UVIS AlpAra035 2aI	2006 DEC 17 23:39:41.31	249.16	149.77	9.49	15.93
UVIS GamPeg036I	2006 DEC 29 09:44:40.71	100.30	318.58	−10.91	5.43
UVIS GamPeg036E	2006 DEC 29 11:56:14.37	159.43	342.81	17.32	10.14
UVIS DelPer036E	2006 DEC 30 17:38:53.66	221.24	291.73	31.79	11.19
VIMS RHya036I	2007 JAN 01 17:09:05.76	194.51	228.95	29.21	5.31
UVIS KapCen036I	2007 JAN 02 16:30:45.73	214.24	236.85	25.48	6.58
UVIS EpsLup036E	2007 JAN 03 12:08:25.00	55.40	125.62	−43.00	−4.89
UVIS DelPer037I	2007 JAN 15 14:11:10.11	25.91	159.76	−0.82	10.94
UVIS EpsLup037I	2007 JAN 20 14:39:04.76	168.95	185.47	1.61	1.48
UVIS EpsLup037E	2007 JAN 20 22:02:04.31	104.34	3.35	−28.94	−5.83
UVIS GamAra037 2E	2007 JAN 22 17:54:12.07	13.07	293.86	−20.08	−23.18
UVIS DelPer039I	2007 FEB 18 18:37:01.73	26.22	62.15	−5.69	−17.63
VIMS alpAur041I	2007 MAR 23 17:32:31.92	7.94	55.67	16.21	−2.90
VIMS RHya041I	2007 MAR 29 07:29:36.59	203.23	279.02	24.80	8.45
UVIS KapCen042I	2007 APR 02 12:37:07.96	300.28	206.57	53.19	6.15
UVIS KapCen042E	2007 APR 02 17:21:51.33	325.78	156.55	−11.59	−6.32
UVIS BetPer042I	2007 APR 08 16:18:52.32	47.48	123.08	−16.70	−10.87
UVIS LamSco044I	2007 MAY 09 12:38:37.41	257.58	70.18	14.03	−1.00
UVIS DelLup057I	2008 JAN 26 22:12:14.52	201.43	222.16	−3.55	−4.11
UVIS ZetCen062E	2008 MAR 22 14:31:27.67	7.73	359.39	−40.26	−10.10
UVIS AlpAra063E	2008 APR 01 11:22:42.65	29.51	211.39	25.92	0.23
VIMS RLeo063I	2008 APR 03 13:15:12.27	98.42	206.48	−0.53	8.79
VIMS RLeo063E	2008 APR 03 13:54:07.75	123.53	221.27	19.15	11.03
UVIS BetCen064E	2008 APR 10 13:35:48.43	335.97	284.67	38.22	10.58
UVIS GamCas064I	2008 APR 11 12:14:23.43	35.84	344.16	−38.22	−3.92
UVIS EpsCen065I	2008 APR 19 11:32:16.70	204.26	347.88	−18.48	31.39
VIMS RCas065I	2008 APR 21 00:44:05.65	30.17	301.76	4.58	−3.66
VIMS CWLeo070I	2008 JUN 03 14:25:16.96	83.33	271.93	35.04	−7.06
VIMS CWLeo070E	2008 JUN 03 16:11:59.11	135.41	295.70	−19.97	−6.72
VIMS gamCru071I	2008 JUN 08 09:08:13.85	186.52	349.32	−79.88	−1.29
VIMS gamCru072I	2008 JUN 15 12:24:05.53	186.12	143.11	−78.23	1.99
VIMS gamCru073I	2008 JUN 22 15:33:07.55	185.78	298.77	−26.62	−2.54
VIMS CWLeo074I	2008 JUL 02 01:07:18.84	92.30	215.17	34.44	−3.79

Table 1 (*continued*)

Event	Time (UTC at Saturn)	λ (°)	$(\lambda - \lambda_M)$[a] (°)	$(r - a)$[b] (km)	Resid.[c] (km)
VIMS CWLeo074E	2008 JUL 02 02:18:39.63	126.36	230.31	63.20	−4.83
UVIS BetCen075I	2008 JUL 06 21:37:44.53	169.36	237.93	72.07	−3.12
VIMS RLeo075I	2008 JUL 09 04:45:34.67	81.38	352.50	−54.18	1.35
VIMS RLeo075E	2008 JUL 09 06:23:52.46	136.60	21.64	3.03	6.26
UVIS BetCen077 1I	2008 JUL 20 23:23:32.94	169.33	262.10	82.71	12.76
UVIS BetCen077 2E	2008 JUL 21 06:44:13.72	28.36	4.24	−74.07	−17.62
VIMS RLeo077I	2008 JUL 23 07:01:27.05	86.05	13.39	−41.15	−7.39
VIMS RLeo077E	2008 JUL 23 08:24:27.21	131.91	37.24	26.48	−10.85
VIMS gamCru078I	2008 JUL 27 20:10:59.31	184.73	174.71	−50.36	2.45
UVIS BetCen078E	2008 JUL 28 07:43:43.98	28.19	194.41	−25.81	10.63
VIMS betGru078I	2008 JUL 28 09:36:33.92	264.65	40.93	44.41	5.41
UVIS AlpAra079I	2008 AUG 04 04:12:15.26	126.74	195.18	−54.22	−20.97
VIMS RSCnc080I	2008 AUG 13 02:06:19.42	57.30	321.29	−64.70	−5.91
VIMS RSCnc080E	2008 AUG 13 07:26:16.26	154.43	333.55	−89.08	0.51
VIMS gamCru081I	2008 AUG 18 06:59:53.39	183.01	259.20	47.29	12.55
UVIS BetCen081I	2008 AUG 18 12:34:40.26	163.73	151.12	−88.12	0.93
VIMS gamCru082I	2008 AUG 25 15:36:26.21	182.66	327.94	−83.73	1.42
UVIS BetCen085I	2008 SEP 16 23:57:31.38	163.10	51.74	62.24	−0.04
UVIS AlpAra085I	2008 SEP 17 09:31:32.78	127.12	223.50	59.08	7.31
UVIS AlpAra085E	2008 SEP 17 12:49:51.25	49.74	93.51	50.96	6.84
VIMS RSCnc085I	2008 SEP 18 22:32:41.08	59.12	286.30	46.01	13.01
VIMS RSCnc085E	2008 SEP 19 03:44:11.61	152.21	296.75	0.28	−17.91
VIMS gamCru086I	2008 SEP 24 03:15:04.11	181.90	224.23	48.18	0.76
VIMS RSCnc087I	2008 OCT 03 16:19:56.69	60.02	56.26	24.26	2.16
VIMS RSCnc087E	2008 OCT 03 21:26:52.90	151.26	66.08	87.62	14.97
VIMS gamCru089I	2008 OCT 16 04:26:21.22	181.68	81.38	52.70	2.64
UVIS BetCen089I	2008 OCT 16 09:56:48.01	163.00	335.03	−72.59	1.78
UVIS AlpAra090I	2008 OCT 24 02:24:07.78	128.22	244.44	33.82	8.89
UVIS AlpAra090E	2008 OCT 24 05:46:20.96	48.62	111.19	24.00	0.32
UVIS BetCen092E	2008 NOV 08 08:54:15.40	21.37	64.30	87.40	−3.80
VIMS RSCnc092I	2008 NOV 10 02:03:09.38	87.38	195.40	−32.14	−1.01
VIMS gamCru093I	2008 NOV 15 16:34:46.64	203.58	330.45	−70.12	8.47
VIMS gamCru094I	2008 NOV 23 01:26:11.87	192.01	24.02	−29.87	−4.07
VIMS epsMus094I	2008 NOV 23 08:27:36.96	259.63	339.85	−88.54	1.38
VIMS epsMus094E	2008 NOV 23 12:54:17.59	314.14	323.62	−61.41	3.39
VIMS gamCru096I	2008 DEC 08 11:48:11.21	187.46	244.72	88.82	−2.87
UVIS BetCen096I	2008 DEC 08 17:50:58.37	166.87	127.90	16.59	4.83
UVIS AlpAra096I	2008 DEC 09 06:25:44.27	115.04	235.85	55.39	−5.43
UVIS AlpAra096E	2008 DEC 09 08:49:52.39	67.85	150.43	−65.18	0.34
VIMS gamCru097I	2008 DEC 16 11:06:07.81	187.36	79.93	94.66	11.59
UVIS DelCen098I	2008 DEC 24 01:37:59.72	194.27	61.70	67.81	−0.80
UVIS BetCru098I	2008 DEC 24 09:10:01.18	219.00	326.52	−21.69	−3.61
UVIS AlpAra098I	2008 DEC 25 07:53:00.37	116.17	222.14	12.59	8.93
UVIS AlpAra098E	2008 DEC 25 10:25:46.44	75.94	141.38	−61.98	1.55
VIMS gamCru100I	2009 JAN 12 10:24:11.75	213.60	243.82	28.63	−0.30
UVIS GamCas100E	2009 JAN 15 13:08:50.14	167.27	87.88	47.68	−6.38
VIMS gamCru101I	2009 JAN 22 00:10:17.00	213.61	186.89	−40.11	30.93
VIMS gamCru102I	2009 JAN 31 13:23:27.05	213.38	138.45	−28.18	17.42
UVIS BetCen102I	2009 JAN 31 20:11:31.47	189.09	5.91	−49.17	−1.58
UVIS BetCen104I	2009 FEB 22 17:08:14.49	225.25	327.14	−11.20	5.74
UVIS BetCen104E	2009 FEB 23 02:31:37.32	339.18	291.62	35.87	−2.87
VIMS betPeg104I	2009 FEB 26 09:05:00.31	353.21	135.37	−32.17	2.96
UVIS BetCen105 1I	2009 MAR 06 16:02:29.20	225.25	80.81	91.41	7.07
UVIS BetCen105 2E	2009 MAR 07 01:26:01.41	339.09	45.16	16.76	5.91
UVIS AlpAra105I	2009 MAR 07 18:13:12.13	136.25	295.15	17.70	−8.03
UVIS AlpAra105E	2009 MAR 08 00:00:17.36	61.92	128.75	−14.55	−1.49
VIMS RCas106I	2009 MAR 22 21:44:07.37	51.80	185.01	−49.44	−6.84
VIMS betPeg108I	2009 APR 05 14:33:32.29	4.07	303.71	34.04	10.16
VIMS alpAur110I	2009 MAY 09 11:47:58.81	315.40	271.40	81.83	−6.29
VIMS alpAur110E	2009 MAY 09 16:45:52.84	243.49	120.47	13.71	−22.09
UVIS ZetCen112I	2009 JUN 12 11:48:34.66	196.41	124.68	13.91	−2.07
UVIS MuCen113I	2009 JUN 26 21:15:04.29	196.01	26.19	−41.03	−8.51
UVIS AlpLup113I	2009 JUN 27 10:53:25.34	232.78	205.88	−45.89	−7.61
UVIS LamSco114I	2009 JUL 14 14:00:18.59	259.75	169.53	−43.23	−0.60
UVIS SigSgr114I	2009 JUL 17 22:06:56.27	186.10	260.85	69.34	−21.22
UVIS AlpVir116I	2009 AUG 11 15:06:30.49	186.32	183.04	−93.23	9.28
UVIS Pi4Ori117E	2009 AUG 27 10:30:35.52	194.45	272.70	57.68	−6.89
UVIS AlpVir124E	2010 JAN 11 13:05:01.58	306.62	212.15	−53.47	9.07
UVIS BetLib124E	2010 JAN 11 14:21:06.69	228.68	114.03	32.09	−7.20
UVIS AlpVir134I	2010 JUL 05 09:43:17.20	142.31	214.38	−50.34	9.07
UVIS BetOri136E	2010 AUG 14 01:30:43.36	234.36	277.59	27.68	7.48
UVIS BetOri138E	2010 SEP 23 00:24:05.98	234.97	136.36	46.01	5.44

[a] Measured longitude relative to the mean longitude of Mimas.

[b] Measured radius relative to the mean value, $a = 117570.0$ km.

[c] Radial residual with respect to our adopted model (see Table 4).

observed in the narrow Uranian rings, where both $m = 0$ and $m = 2$ modes are seen in the γ and δ rings, as well as the more familiar $m = 1$ modes (French et al., 1988, 1991). The difference here is that the modes exist at the edge of the broad B ring, rather than spanning a narrow ring.

In the present paper, our goal is to re-examine the entire suite of occultation data for the B ring edge, in light of the results obtained by Spitale and Porco (2010) and with a particular view to clarifying the issue of libration vs. circulation. In addition to the *Cassini* VIMS and RSS data and the historical *Voyager* and Earth-based occultation data, we augment the dataset used by Hedman et al. (2010a) with an additional 8 VIMS occultations and an extensive set of *Cassini* UVIS occultations from 2005 through 2009, as described by Colwell et al. (2010). Our models for the B ring edge—which are completely independent of the imaging data—turn out to be largely consistent with the results of Spitale and Porco (2010). Apart from the value of an independent analysis based on a different dataset, the much longer temporal baseline of the occultation data (~30 yrs vs. 4 yrs) permits more accurate estimates of the key mode frequencies than is possible with *Cassini* imaging data alone.

After a brief review of the observational data in Section 2, and a more complete description of our dynamical model in Section 3, we present our results in Sections 4 and 5. Our conclusions are summarized in Section 6, together with the status of the 'resonant-cavity' model for the outer B ring.

2. Observations

Our data set includes all known occultation measurements of the outer edge of the B ring, beginning with the *Voyager* observations in 1980 and 1981. Since the majority of the measurements are identical to those described by French et al. (2010) and Hedman et al. (2010a), we give only a brief overview in this section.

2.1. Historical data

French et al. (2010) provide a complete set of measured B ring radii from the *Voyager* 1 RSS occultation, the *Voyager* 2 PPS occultation, ground-based observations of the 28 Sgr occultation in 1989, and the HST occultations in 1991 and 1995, in their Table 5. The *Voyager* event times are taken from the measurements of French et al. (1993), with the PPS timing calibration of Nicholson et al. (1990). Ring plane radii and longitudes were recomputed using updated values for the Saturn pole direction and revised spacecraft ephemerides (Jacobson, 2003).

For the 28 Sgr data, measured times were also taken from the work of French et al. (1993), using data from Palomar, McDonald, the IRTF and the ESO 1 and 2 m telescopes. Again, ring plane radii and longitudes were recomputed using updated values for the Saturn pole direction and revised stellar coordinates from *Hipparcos*.

Both HST data sets were reanalyzed by French et al. (2010), using the latest instrumental calibrations and updated stellar coordinates, to determine the radii of all recognizable sharp features. We use their three measurements of the B ring edge, two in 1991 and one in 1995.

For both the 28 Sgr and HST data, uncertainties in the Saturn ephemeris, errors in the positions of the occulted stars and possible timing errors between the various telescope clocks were accommodated by solving for corrections to the stellar right ascensions and declinations, $\Delta\alpha_*$ and $\Delta\delta_*$, as well as differential timing offsets between observatories. These solutions were constrained by adopting the radii determined by French et al. (1993) for an ensemble of circular ring features. Final systematic radius errors are estimated at 1 km or less.

2.2. Cassini radio occultation data

Between May and September 2005 the *Cassini* RSS team observed a total of twelve radial occultations by the rings, at three frequencies and in several cases at multiple ground stations. We use 12 independently-measured event times for the B ring edge from Table 5 of French et al. (2010) to compute radii and longitudes. Internal errors, as measured by the consistency of results for a given occultation across multiple ground stations, are estimated at much less than 100 m, but comparisons of the radii of what are believed to be circular features between different occultations and between ingress and egress cuts of the same occultation yielded typical residuals of 0.5–1 km. This is probably due to errors in the reconstructed spacecraft trajectory, and after applying timing offsets to each occultation, French et al. (2010) reduced the rms residuals with respect to Keplerian orbital fits for many ring features to ~250 m.

We have compensated for these same errors by applying a small timing offset to each RSS occultation, such as to minimize the radius residuals for the same five circular features identified by Hedman et al. (2010a), namely the outer edges of the Russell, Jeffreys, Kuiper, Bessel and Barnard gaps. With these corrections, the rms residuals for these five reference features fell to between 150 and 270 m. The mean radii of these same features, obtained from the two-sided occultation on orbit 11, agreed with those given by Hedman et al. (2010a) to within 100 m in all cases.

2.3. Cassini stellar occultation data

In their previous analysis of features in the Cassini Division, including the outer edge of the B ring, Hedman et al. (2010a) used data from ~40 stellar occultations observed by the *Cassini* VIMS instrument between April 2005 and December 2008. A list of the individual observations is given in their Table 1, with the corresponding star positions in Table 2. For the present analysis, we have remeasured all of the B ring and sharp Cassini Division edges in these data, using the same RINGMASTER software developed by French et al. (2010) to process the HST and RSS data. In addition, we have included data from 8 subsequent occultations through May 2009. Typical internal errors are estimated to be of order 400 m, based on sampling intervals of 20–80 ms and projected spacecraft velocities of 5–10 km s^{-1}.

Since *Cassini* entered Saturn orbit in July 2004, the UVIS instrument has observed over 100 stellar occultations by the rings, many of which crossed the B ring edge (Colwell et al., 2010). As part of a larger project to understand the overall geometry of the rings, we have measured all of these crossings, again using the RINGMASTER software, and converted the resulting event times to radii and longitudes in Saturn's ring plane. Typical internal errors are expected to be as small as 20 m, based on sampling intervals of 1–4 ms, considerably less than likely errors in the reconstructed trajectory.

For each VIMS and UVIS occultation, the radii of the same five circular reference features used to adjust the RSS profiles were measured and compared to their nominal RSS values. In most cases the rms differences were ~500 m, but there were several cases where systematic offsets as large as several km were found, which we again attribute to spacecraft trajectory errors. (Note that for oblique viewing geometries, a small error in the spacecraft position can result in a much larger error in the calculated ring plane radius.) Just as for the RSS data, we computed a timing offset for each stellar occultation such as to minimize the radius residuals for the five circular reference features identified by Hedman et al. (2010a). After this correction, the rms residuals dropped to

250 m or less in almost all cases. We found no significant difference between the rms radius residuals for these two instruments, despite the shorter integration times of the UVIS data. Because of structure in the ring profiles—even the sharpest edges have intrinsic widths of at least 100 m (Jerousek et al., 2011)—it is difficult to define edge locations to better than this level, even for data with very high signal-to-noise ratio and/or sampling rate.

2.4. Data catalog

Our complete data set is presented in Table 1, where we list the occultation event time (UTC at Saturn), the inertial longitude and the longitude relative to that of Mimas, and the measured radius of the B ring edge relative to a mean value of 117570.0 km. Also listed are the radius residuals with respect to our adopted model, which is documented in Table 4 below. This catalog will be made available via NASA's Planetary Data System.

3. Dynamical model

Our model of the $m = 2$ perturbation is based on the classical model for the motion of a test particle in the neighborhood of a first-order inner Lindblad resonance, as described by Hedman et al. (2010a). At the exact resonant radius, $a_{\rm res}$ we have

$$(m-1)n + \dot{\varpi}_{\rm sec} - mn_s = 0, \tag{2}$$

where m is a positive integer, n and n_s are the orbital mean motions of the ring particle and satellite, respectively, and $\dot{\varpi}_{\rm sec}$ is the apsidal precession rate of the ring particle due to non-resonant perturbations (chiefly the planet's oblateness). For a 2:1 ILR, $m = 2$ and $n_{\rm res} = 2n_s - \dot{\varpi}_{\rm sec}$. Following Eq. (14) in Hedman et al. (2010a), the perturbed orbits of the ring particles are given by

$$\Delta r_2(\lambda, t) \approx -ae_2(t)\cos[2(\lambda - \lambda_M) - \phi_2(t)], \tag{3}$$

where λ_M is the mean longitude of Mimas at time t and the parameters e_2 and ϕ_2 are slowly-varying functions of time. Geometrically, Eq. (3) describes a 2-lobed radial distortion rotating at the same average rate as the satellite, but with a minimum displaced by an angle $\phi_2(t)/2$ ahead of the satellite's mean longitude. (This is identical to Eq. (1) above, but here and henceforth we add the subscript "2" to e and ϕ in order to distinguish the $m = 2$ perturbation from other components to be discussed below.)

At a first-order ILR, such as the Mimas 2:1 resonance, the resonance variable ϕ_m is defined as

$$\phi_m = (m-1)\lambda + \varpi - m\lambda_s, \tag{4}$$

where λ and λ_s are the mean longitudes of the ring particle and satellite, respectively, and ϖ is the longitude of pericenter of the ring particle's orbit. From Eq. (2), we see that, in the neighborhood of $a_{\rm res}$, $d\phi_m/dt \approx 0$.

Following the dynamical model outlined by Hedman et al. (2010a), and illustrated in Fig. 1 above for orbits interior to the resonant radius, the slow variations in e_2 and ϕ_2 are given by

$$e_2\cos\phi_2 = e_0 + e_f\cos(\Omega_L t - \delta_L) \tag{5}$$

$$e_2\sin\phi_2 = e_f\sin(\Omega_L t - \delta_L), \tag{6}$$

where Ω_L is the libration (or circulation) frequency and δ_L is an arbitrary constant that sets the phase of libration. The free parameters of the $m = 2$ model are thus Ω_L and δ_L, in addition to the forced and free eccentricities e_0 and e_f, and the mean radius a. As noted already in Section 1, if $e_f < e_0$ the motion is a libration about $\phi_2 = 0$, while if $e_f > e_0$ the phase angle circulates continuously through 2π radians.[2]

Based on the simple test-particle model described in Hedman et al. (2010a), we would expect that e_0 is determined by the distance of the B ring edge from the exact resonance location, $a - a_{\rm res}$. Substituting appropriate numerical values for the Mimas 2:1 resonance, we find that

$$ae_0 \approx 450\left(\frac{1\text{km}}{|a - a_{\rm res}|}\right)\text{km}. \tag{7}$$

Similarly, the libration frequency should be given by the expression

$$\Omega_L \approx -0.0097^\circ\left(\frac{a - a_{\rm res}}{1\text{ km}}\right)\text{ d}^{-1}. \tag{8}$$

For modeling purposes, however, we will treat these two quantities as free parameters.

As demonstrated by Spitale and Porco (2010), this model is mathematically equivalent to a superposition of a forced $m = 2$ distortion with amplitude ae_0 locked to Mimas and rotating at an angular rate n_M plus a free $m = 2$ mode with an amplitude ae_f rotating at a slightly different rate Ω_2. The libration frequency is given by the beat frequency between these two modes, $\Omega_L = 2(\Omega_2 - n_M)$, where the factor of 2 arises because there are two minima in each pattern.

In addition to the $m = 2$ perturbation, our B ring edge model includes terms describing other free normal modes of oscillation:

$$\Delta r_m(\lambda, t) \approx -ae_m\cos[m(\lambda - \Omega_m t - \delta_m)], \tag{9}$$

where ae_m and δ_m are the mode's radial amplitude and phase, respectively. For each value of m, the pattern speed Ω_m is expected to be close to that of an ILR located at the particles' orbit (French et al., 1991), i.e.,

$$\Omega_m \simeq [(m-1)n + \dot{\varpi}_{\rm sec}]/m, \tag{10}$$

where n is the local orbital angular velocity and $\dot{\varpi}_{\rm sec}$ is the apsidal precession rate due to the planet's zonal gravity harmonics. For each mode, the additional fit parameters are conveniently specified by e_m, Ω_m and δ_m. Note that an $m = 1$ mode is equivalent, to first order in e, to a Keplerian ellipse freely-precessing under the influence of the planet's zonal gravity harmonics and in this case we use the exact expression

$$r_1(\lambda, t) = \frac{a(1 - e_1^2)}{1 + e_1\cos(\lambda - \Omega_1 t - \delta_1)}. \tag{11}$$

Here $\Omega_1 \simeq \dot{\varpi}_{\rm sec}$ and $\delta_1 = \varpi_0$, the longitude of pericenter at $t = 0$.

Our nominal model, written as

$$r(\lambda, t) = r_1(\lambda, t) + \Delta r_2 + \sum_{m>2}\Delta r_m, \tag{12}$$

thus has at least 11 free parameters: a mean radius, a, four parameters to describe the librating or circulating $m = 2$ mode, and three each for the $m = 1$ and $m = 3$ normal modes. We have also carried out fits including additional free modes, up to and including $m = 8$. For some fits, we add a constant offset $\delta\lambda$ to the longitude of Mimas to allow for the possibility of an offset in the forced eccentricity of the ring edge relative to Mimas. This is equivalent to applying a constant offset to the phase variable, ϕ_2.

Mimas' long-term mean motion is 381.994509° d^{-1} (Harper and Taylor, 1993). In implementing the $m = 2$ model over a time span of almost 30 yrs, however, it is necessary to include the influence of the Mimas-Tethys 4:2 resonance on the mean longitude of Mimas, which oscillates with an amplitude of 43.7° and a period of 70.8 yr relative to what would be calculated assuming a constant mean motion. As a result, the satellite's mean motion varies by ±0.0106° d^{-1} over the same period. The phase of this libration is such that Mimas' mean motion reached its minimum value of ~381.9835° d^{-1} in mid-2007, and has varied relatively little during the 2005–2010 span of *Cassini* observations used here. This is the

---

[2] A similar description applies to orbits exterior to the resonant radius, but with clockwise motion about a fixed point at $\phi_2 = \pi$. See Hedman et al. (2010a) for details.

Table 2
Least-squares fit model parameters.[a]

Fit #	Dataset	N[b]	Ω_L[c] ($^\circ$ d^{-1})	ae_0[c] (km)	ae_f[c] (km)	Ω_1 ($^\circ$ d^{-1})	ae_1 (km)	Ω_3 ($^\circ$ d^{-1})	ae_3 (km)	σ[d] (km)
1	*Cassini*	133	0.1654	37.3	40.0					20.44
2	All	146	0.1817	37.3	38.8					20.63
3	*Cassini*	133	0.1833	33.6	37.5	[5.0980]	20.1	[507.7000]	13.1	10.21
4	All	146	0.1805	35.9	37.8	[5.0980]	17.6	[507.7000]	13.0	12.05
5[e]	*Cassini*	133	0.1842	33.4	37.0	5.0714	20.7	507.7001	12.9	9.73
6[f]	All	146	0.1819	34.4	36.9	5.0835	20.6	507.7027	13.3	9.83
7[g]	*Cassini*	133	0.1858	33.2	36.8	5.0710	20.6	507.7003	13.0	9.76
8[g]	All	146	0.1820	34.4	36.7	5.0835	20.5	507.7028	13.3	9.86
9	No Vgr	144	0.1823	34.1	37.1	5.0832	20.4	507.7021	13.1	9.85
10	No HST	143	0.1820	34.3	36.8	5.0843	20.8	507.7022	13.4	9.71
11[h]	*Cassini*	133	0.1808	33.4	37.0	5.0807	20.4	507.6998	12.4	7.81
SP2010[i]			0.179	34.6	37.3	5.098	20.9	507.700	11.8	7.9

[a] Values in [$\cdots$] were held fixed.
[b] Number of data points fitted.
[c] $m = 2$ model parameters.
[d] Post-fit rms residual per degree of freedom.
[e] Nominal fit to *Cassini* data. See Table 3 for full parameter set.
[f] Nominal fit to all data. See Table 4 for full parameter set.
[g] Fit includes phase lag in $m = 2$ forced mode with respect to Mimas, $\delta\lambda$ (see text).
[h] Fit includes $m = 4$ and 5 modes; see Table 5 for full parameter set.
[i] Fit parameters from Spitale and Porco (2010).

Table 3
Three-mode fit to *Cassini* data (fit 5).

Parameter	Symbol	Value
Mean radius	a (km)	117570.42 ± 0.86
Forced $m = 2$ mode	ae_0 (km)	33.40 ± 1.51
Free $m = 2$ mode	ae_f (km)	37.04 ± 1.24
	Ω_L ($^\circ$ d^{-1})	0.1842 ± 0.0046
	δ_L ($^\circ$)	100.14 ± 2.02
Epoch		TDB 2008 Jan 1 12:00
RMS resid per DoF	σ (km)	9.731
# Data	N	133

m	ae_m (km)	Ω_m ($^\circ$ d^{-1})	δ_m ($^\circ$)
1	20.70 ± 1.22	5.0714 ± 0.0071	68.17 ± 3.49
3	12.94 ± 1.25	507.7001 ± 0.0038	19.40 ± 1.80

Table 4
Adopted model: three-mode fit to all data (fit 6).

Parameter	Symbol	Value
Mean radius	a (km)	117570.12 ± 0.85
Forced $m = 2$ mode	ae_0 (km)	34.38 ± 1.35
Free $m = 2$ mode	ae_f (km)	36.94 ± 1.19
	Ω_L ($^\circ$ d^{-1})	0.1819 ± 0.0012
	δ_L ($^\circ$)	100.46 ± 2.03
Epoch		TDB 2008 Jan 1 12:00
RMS resid per DoF	σ (km)	9.831
# Data	N	146

m	ae_m (km)	Ω_m ($^\circ$ d^{-1})	δ_m ($^\circ$)
1	20.59 ± 1.19	5.0835 ± 0.0016	68.54 ± 3.52
3	13.31 ± 1.21	507.7027 ± 0.0014	19.56 ± 1.74

same (constant) value adopted for n_M by Spitale and Porco (2010) for their work. Neglecting the Mimas-Tethys libration over the longer period of the occultation data, however, could lead to errors in the calculated value of λ_M of as much as $\sim 80^\circ$.

In order to separate this signature from the numerous short-period perturbations in longitude due to Mimas' eccentric orbit, we extracted Mimas' instantaneous state vector from the numerical JPL ephemerides and then converted this to epicylic orbital elements using the prescription of Renner and Sicardy (2006). These elements include the mean longitude, shorn of all short-term variations. As a test of this procedure, we compared the epicyclic mean motion with the analytic expression for the Mimas-Tethys libration given by Harper and Taylor (1993), finding excellent agreement.

Our model has several theoretical limitations and we regard it primarily as an empirical fit to the occultation data, albeit one motivated by the known resonance dynamics. We have made little attempt to include out-of-plane distortions,[3] although *Cassini* images obtained near Saturn's equinox in mid-2009 show clear evidence for *local* vertical distortions of several hundred meters amplitude (Spitale and Porco, 2010). Although our model is based on a dynamical description of the response to the 2:1 Mimas ILR for an *isolated* ring particle, it does not include the effects of gravitational and collisional interactions between ring particles. Almost certainly, these interactions will modify the amplitude and the phase of the perturbations forced by Mimas, and possibly also the libration frequency Ω_L, relative to those predicted by the test-particle model. It is for this reason that we choose to treat the quantities Ω_L and e_0 as free parameters in the fits, rather than attempting to calculate Ω_L from $a - a_{\rm res}$ and Eq. (8), or requiring e_0 to satisfy Eq. (7).

Finally, we note that the epoch adopted for our fits, namely 2008 Jan 1, 12:00 TDB at Saturn, was chosen to approximate the mid-time of the *Cassini* occultation dataset and differs from the epochs used by Hedman et al. (2010a) and Spitale and Porco (2010). This choice has the desirable effect of minimizing cross-correlations between the various fit parameters. The choice of epoch affects only the phase angles, δ_L and δ_m.

4. Results

4.1. Least-squares fits

All of our orbit fits were carried out using a well-tested nonlinear least-squares routine, based on the Leavenberg–Marquardt algorithm. This routine is essentially that same as that used by French et al. (1988) for their fits to Uranian ring occultation data, by French et al. (1993) to fit the 28 Sgr data for Saturn's rings, and most recently by French et al. (2010) to study features in the Cassini Division. The underlying geometric model is the heliocentric calculation documented in Appendix B of French et al. (1993). All necessary

---

[3] A simple fit for a constant inclination, with an appropriate nodal regression rate, yielded a null result.

planetary and spacecraft ephemeris data were obtained from SPICE kernels generated for the *Cassini* project, and stellar positions were taken from the *Hipparcos* catalog (where available), and corrected for proper motion and parallax at Saturn. For additional details pertaining to the *Voyager*, 28 Sgr and HST occultations, including the various station time offsets, etc., see Table 1 in French et al. (2010).

For all fits presented here, the data are *unweighted*, i.e., all data points are assigned equal weight, even though the original measurement uncertainties vary substantially. Our rationale for this is as follows. Given the estimated errors, as reviewed in Section 2, a 'good' fit would be expected to have a post-fit rms residual per degree of freedom of order 1 km or less, if our model includes all relevant perturbations. Indeed, our fits to most other sharp-edged features in the C ring and Cassini Division yield values of σ in the range 0.3–1.0 km (French et al., 2011; Nicholson et al., 2011). However, none of our B ring edge fits approaches this ideal, and typical post-fit residuals are 7–10 km. This is comparable to the residuals found by Spitale and Porco (2010) for their fits to the *Cassini* imaging data. This by itself indicates that the deviations from the fits are model-related, not data-related, and that under these circumstances, we have no reason for weighting some observations more heavily than others based on their *measurement* uncertainties. In this circumstance, we evaluate our χ^2 statistic using the post-fit rms residual per degree of freedom, σ, rather than scaling each individual residual by its own measurement uncertainty. More specifically,

$$\chi^2 = \sum_{1}^{N} \frac{(r_{\rm obs} - r_{\rm calc})^2}{\sigma^2}, \qquad (13)$$

where N is the number of data points (typically $\sim$140) and σ is chosen to make χ^2 for the best fit equal to $N - N_p$, where N_p is the number of fit parameters.

The uncertainties quoted for our model parameters have been chosen so that they correspond to an increase in χ^2 of 1.0 relative to its minimum value of $N' = N - N_p$, where N' is number of degrees of freedom in the fit (Bevington and Robinson, 2003).

Although our final fit includes all 11 free parameters as described in Section 3 above, and all the available occultation data, we also carried out an extensive series of fits using subsets of the data and/or a simpler kinematic model in order to test the robustness of our results. We present a summary of the more interesting of these fits in Table 2, including the best-fitting $m = 2$ libration frequency Ω_L, the pattern speeds $\Omega_1 = \dot\varpi$ and Ω_3, the corresponding radial amplitudes ae_0, ae_f, ae_1 and ae_3, and the post-fit rms residual σ. After an overview of all the fits, we discuss the individual components of the B ring edge perturbations in Sections 4.2–4.5 below.

Table 5
Five-mode fit to *Cassini* data (fit 11).

Parameter	Symbol	Value
Mean radius	a (km)	117570.18 ± 0.70
Forced $m = 2$ mode	ae_0 (km)	33.38 ± 1.24
Free $m = 2$ mode	ae_f (km)	37.05 ± 0.99
	Ω_L (° d^{-1})	0.1808 ± 0.0040
	δ_L (°)	100.60 ± 1.68
Epoch		TDB 2008 Jan 1 12:00
RMS resid per DoF	σ (km)	7.808
# Data	N	133

m	ae_m (km)	Ω_m(° d^{-1})	δ_m (°)
1	20.44 ± 0.99	5.0807 ± 0.0061	68.49 ± 2.97
3	12.45 ± 1.03	507.6998 ± 0.0034	19.02 ± 1.53
4	5.94 ± 1.01	570.5088 ± 0.0056	1.31 ± 2.44
5	5.62 ± 0.99	608.1980 ± 0.0047	65.04 ± 2.16

For our initial fits we included only the $m = 2$ distortion, as described by Eqs. (3)–(6), and set the Mimas phase lag $\delta\lambda = 0$. Fit 1 includes *Cassini* data only, while fit 2 includes all the available occultation data, going back to 1980. Both fits yield rms residuals of $\sim$20 km, indicating that a pure $m = 2$ model—even one that allows for libration or circulation of the resonant variable ϕ_2—cannot provide a very satisfactory fit to the data. Inspection of the individual residuals in fit 2 shows a maximum of 50 km, with 17 data points lying 30 km or more from the best-fitting $m = 2$ model. One of the largest deviations (−39 km) is for the *Voyager 1* RSS point. The best-fitting libration frequencies, Ω_L for these fits are similar to that obtained by Spitale and Porco (2010), given in the last row of Table 2, but differ by almost 10% between the two fits.

We next included both $m = 1$ and $m = 3$ normal modes, initially keeping the values of the pattern speeds Ω_1 and Ω_3 fixed at those found by Spitale and Porco (2010) while scanning over a wide range of values for the libration frequency Ω_L.[4] With rms residuals of 10 and 12 km, these fits (3 and 4) are much improved over the pure $m = 2$ models, but the fit including pre-*Cassini* data is significantly poorer, suggesting that the pattern speeds are in need of some adjustment. In both cases, $\Omega_L \simeq 0.182°\ {\rm d}^{-1}$.

We then turned our attention to optimizing Ω_1 and Ω_3. The improvement in the fit to the full dataset (fit 6) is quite noticeable, with a post-fit rms residual of 9.83 km that is now only slightly greater than that of the *Cassini*-only solution (fit 5). This was accomplished primarily by decreasing the $m = 1$ pattern speed from 5.098 to 5.0835 ± 0.0016° d^{-1}, while increasing ae_1 from 17.6 to 20.6 ± 1.2 km. (Ω_3 was only slightly increased, with a negligible change in ae_3.) The best-fitting $m = 2$ libration frequency, $\Omega_L = 0.1819°\ {\rm d}^{-1}$, is almost unchanged from fit 2. The largest two individual residuals are now 30 km each; all but these two data points now fall within 23 km of the model. Fitting the *Cassini* data alone (fit 5 in Table 2), we obtained an even lower value of $\Omega_1 = 5.0714 \pm 0.0071°\ {\rm d}^{-1}$, but the post-fit residual of 9.73 km is only slightly improved over fit 3. Further details concerning the $m = 1$, 2 and 3 modes are given in Sections 4.2,4.3 and 4.4 below.

Although we shall adopt fits 5 and 6 as the best 3-mode fits to the occultation data, and document these more fully in Tables 3 and 4, we did try several variants on these fits in order to test some of our built-in assumptions and to investigate whether our fits might be unduly influenced by any particular subset of the pre-*Cassini* data.

For all of the fits above, we used the epicyclic mean longitude of Mimas in Eq. (3), calculated as described in Section 3, so as to include its long-term variations due to the resonance with Tethys. As an experiment, we instead tried fixing Mimas' mean motion at the long-term average value determined by Harper and Taylor (1993). Such a model would be valid if the ring edge responds only to the very long-term motion of Mimas, and somehow ignores its 70-yr resonant libration. Perhaps not surprisingly, this fit is significantly worse than fit 6, with an rms residual of 14.2 km. This particular fit is not included in Table 2.

Our next experiment was to include a constant offset in the longitude of Mimas, $\delta\lambda$, as described in Section 3 above. Such an offset — in reality a positive value of this would represent a delay in the time of the ring's forced response to Mimas' perturbation—might be expected to arise from collisional dissipation within the B ring. However, fits to the *Cassini* data alone (fit 7) and to the full dataset (fit 8) both yielded statistically insignificant offsets of $\delta\lambda \simeq -0.7 \pm 1.1°$. (A slight *increase* in the rms residual per degree of freedom is due to the reduction in the number of degrees of freedom by 1, with no corresponding reduction in the sum of

---

[4] All other parameters, including the 4 amplitudes and 3 phases (δ_1, δ_L and δ_3) were adjusted to provide the best fit at each value of Ω_L.

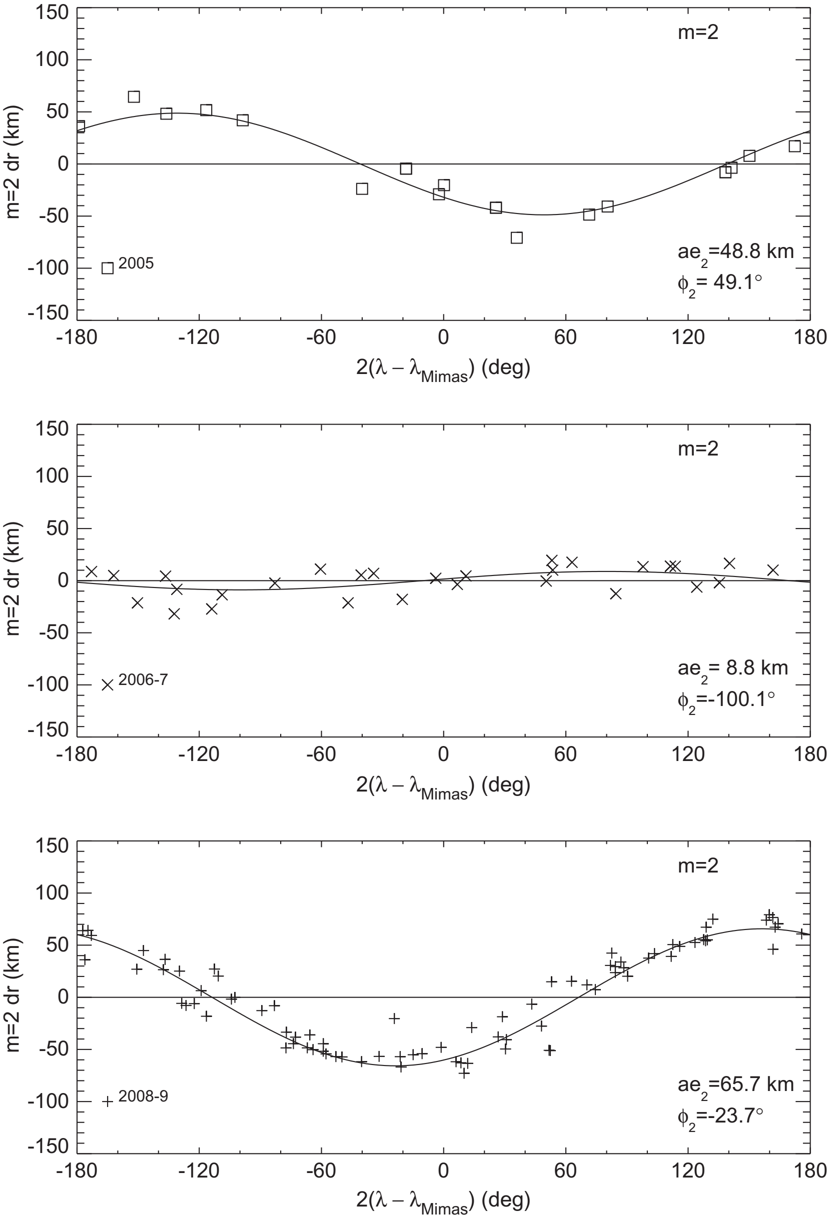

Fig. 2. The distribution of *Cassini* occultation data relative to the best-fitting 3-mode model (fit 6 in Table 2). Each panel shows the $m = 2$ pattern, after removal of the best-fitting $m = 1$ and $m = 3$ perturbations, plotted as a function of $2(\lambda - \lambda_M)$, along with a model curve for the slowly-varying $m = 2$ perturbation. The data are separated into three natural groups, for 2005, 2006/2007 and 2008/2009. The amplitude reached a minimum in late 2006.

squared residuals.) Our negative result differs from that of Spitale and Porco (2010), who found a lag in the ring's forced $m = 2$ response of 2.9 ± 0.3° at their fit epoch of JED 245 4256.9 = 2007 June 5, 09:36. (We explored the possibility that Spitale and Porco used Mimas' true longitude for their reference point, instead of its mean longitude, which can lead to a discrepancy of up to $\pm 2e_M = \pm 2.3°$, but this would have made their derived lag even larger.).

We also ran several tests to see if our fits might be strongly influenced by any particular subset of pre-*Cassini* data, excluding either the *Voyager* or HST data in turn. Fit 9 omits the two *Voyager* occultation points, one of which had proven particularly troublesome in fit 2. The rms residual with respect to fit 6 is virtually unchanged at 9.85 km, as are the $m = 1$, $m = 2$ and $m = 3$ pattern speeds. In fit 10 we omit the three HST points, two from the 1991 occultation and one from November 1995. These three data show some of the largest residuals in fit 6, although both events were recently reanalyzed by French et al. (2010). Again the parameters of the fit are almost unchanged from those of fit 6, although in this case the rms residual is reduced slightly to 9.71 km. We conclude that while the HST data do not significantly influence our final fit parameters, they do contribute disproportionately to the post-fit residuals.

Our final step (fit 11) was to see if additional global oscillation modes might improve the fit to the occultation data. Searches for normal modes up to $m = 8$ revealed what appear to be significant signatures for $m = 4$ and 5, with best-fitting amplitudes of 5–6 km and pattern speeds very close to those predicted by Eq. (10) above. Further details are given in Section 4.5 below. But even with these two additional components—and 6 new free parameters in the fit—the post-fit rms residuals are only reduced to 7.81 km. We thus conclude, in agreement with Spitale and Porco (2010), that a large part of the residuals must represent real but unmodelled structure on the edge of the B ring.

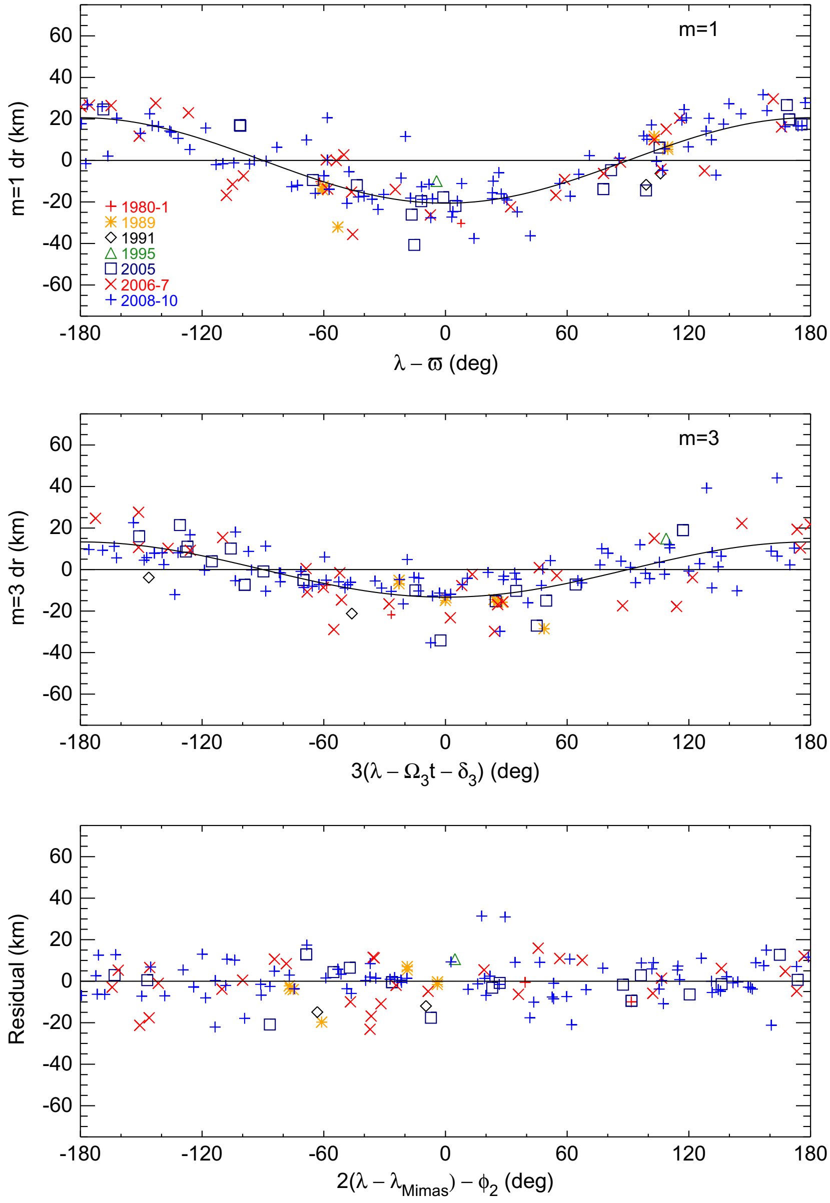

Fig. 3. The distribution of all occultation data relative to the best-fitting 3-mode model (fit 6 in Table 2), after removal of the $m = 2$ perturbations. The upper panel shows the residuals as a function of $\lambda - \varpi$, after also subtracting the $m = 3$ perturbation, along with the model curve for the $m = 1$ perturbation. The different symbols correspond to different observation periods, as denoted in the legend. The middle panel shows the residuals after also subtracting the best-fitting $m = 1$ perturbation, plotted as a function of $3(\lambda - \Omega_3 t - \delta_3)$, along with the model curve for the $m = 3$ perturbation. The lower panel shows the residuals after removing all three perturbations, as a function of the phase of the main $m = 2$ perturbation. The rms deviation is 9.83 km, but some individual residuals are as large as +30 or −20 km.

Fit 11 is our best 5-mode fit to the *Cassini* data alone. A complete description of this fit is provided in Table 5. For reasons discussed in Section 4.5, we do not provide a corresponding 5-mode fit to the full data set. We adopt fit 6 (Table 4) as the best overall fit to the entire data set. In Figs. 2 and 3, we plot the residuals of this fit, and show the separate contributions of the $m = 1$, 2 and 3 modes to the overall distortion of the B ring edge.

In Fig. 2 we show the *Cassini* data from 2005, 2006/2007 and 2008/2009 separately, plotted as a function of $2(\lambda - \lambda_M)$, after subtracting the contributions from the $m = 1$ and $m = 3$ modes. The smooth curves show the predicted $m = 2$ perturbation, based on the fitted values of e_0, e_f, Ω_L and δ_L. Several aspects of this figure are noteworthy, and reinforce conclusions drawn by previous authors (Esposito et al., 2009; Hedman et al., 2010a; Spitale and Porco, 2010). First is the strongly-variable amplitude of the $m = 2$ perturbation, which varies from ~50 km in 2005 to ~10 km in 2006/2007 and ~65 km in 2008/2009. Second is the phase of the radial minimum relative to Mimas, which shifts from leading the satellite by ~25° in 2005 (i.e., $\phi_2 = 49°$) to trailing by ~12° in 2008/2009 (i.e., $\phi_2 = -24°$). Both the amplitude and phase variations can be understood geometrically in terms of Fig. 1, noting that the total eccentricity vector passed very near the origin (i.e., $e_2 = 0$) in late 2006.

The top panel of Fig. 3 shows the entire data set, plotted as a function of $\lambda - \Omega_1 t - \delta_1 = \lambda - \varpi$, after subtracting the contributions from the $m = 2$ and $m = 3$ modes. The smooth curve shows the predicted $m = 1$ perturbation, based on the fitted values of $e_1, \dot{\varpi}$ and ϖ_0. Similarly, the middle panel of Fig. 3 shows the entire data set, plotted as a function of $3(\lambda - \Omega_3 t - \delta_3)$ after subtracting the contributions from the $m = 2$ and $m = 1$ modes. The smooth curve shows the predicted $m = 3$ perturbation, based on the fitted values of e_3, Ω_3 and δ_3. The lower panel of Fig. 3 shows the entire data set,

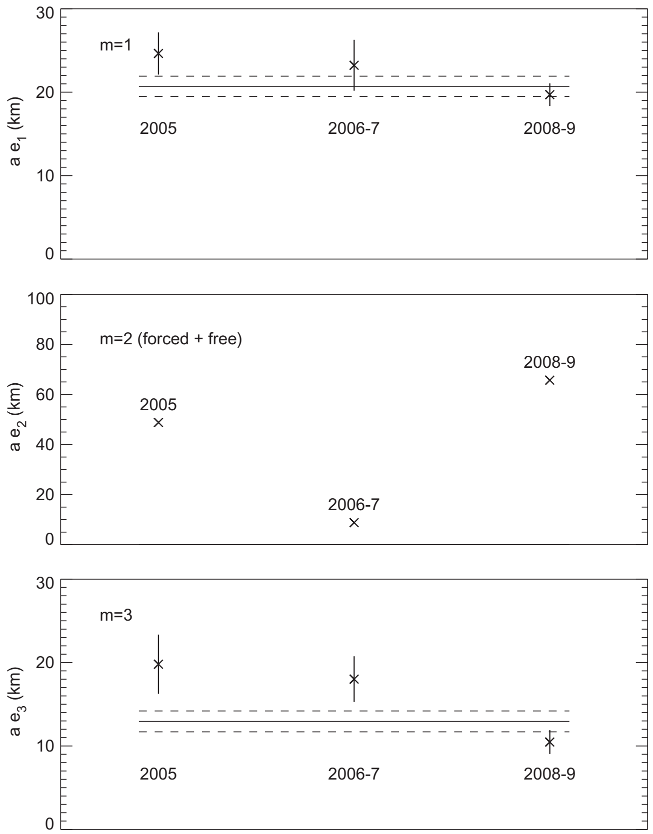

Fig. 4. The variation in amplitudes of the $m = 1$, 2 and 3 modes over the span of *Cassini* occultation data. The $m = 1$ and $m = 3$ amplitudes fitted to each subset of data in Fig. 2 are shown as crosses with error bars, while the corresponding $m = 2$ amplitudes (without error bars) are calculated from the libration parameters e_0 and e_f via Eqs. (5) and (6). Horizontal solid and dashed lines indicate the best-fitting mean values of ae_1 and ae_3 and their 1σ uncertainties from Table 3.

plotted as a function of $2(\lambda - \lambda_M) - \phi_2$, after subtracting the contributions from all three fitted modes.

Note in particular the satisfactory agreement between data and model for both *Voyager* points (red crosses), the two HST points from 1991 (black diamonds), the single HST datum from 1995 (green triangle) and the 28 Sgr data (orange asterisks). One of the 28 Sgr points remains far from the model, with a post-fit residual of -20 km, but this is no longer significantly worse than several of the *Cassini* residuals.

Given the large variation in the amplitude of the $m = 2$ mode over the span of Cassini observations seen in Fig. 2, it might be asked whether the $m = 1$ and/or $m = 3$ modes show similar variations, perhaps correlated or anticorrelated with the dominant mode. Although the present dataset is insufficient to permit full 11-parameter fits to subsets of the data, we have carried out fits for the amplitudes, ae_1 and ae_3 and phases, δ_1 and δ_3 to the three subsets of data shown in Fig. 2, while keeping the pattern speeds, Ω_1 and Ω_3, fixed at the values in Table 3. The results are shown in Fig. 4, where we also plot the variation in ae_2 derived from the resonant model parameters e_0 and e_f. While there is no direct correlation between either the $m = 1$ or $m = 3$ amplitude and that of the $m = 2$ mode, there does seem to be a significant long-term decline in ae_3 from 19.8 ± 3.6 km in 2005 to 10.5 ± 1.4 km in 2008–2009. A less-marked decrease in ae_1 is also indicated, from 24.6 ± 2.5 km to 19.7 ± 1.4 km, but this is only barely statistically significant.

In the next four subsections we discuss the pattern speeds for the individual modes and compare them with the results of Spitale and Porco (2010).

4.2. The $m = 2$ pattern

4.2.1. Libration vs circulation?

One of the principal motivations for this study was to clarify the issue of libration vs circulation for the dominant $m = 2$ perturbation. Fig. 2 confirms that the amplitude of the $m = 2$ perturbation was indeed very small in late 2006 and early 2007, but by itself this does not favor either libration or circulation; as illustrated in Fig. 1, this simply implies that the forced and free eccentricities are very similar. If one could determine the *phase* of the perturbation at this time, then a clear distinction is possible: $\phi \simeq 0$ would imply that $e_f < e_0$ (i.e., libration) while $\phi \simeq 180^\circ$ would imply that $e_f > e_0$ (i.e., circulation). But since we have relatively few occultations at this critical period, and the amplitude is small, it does not seem practicable to determine the phase directly.

Instead, we must rely on our estimates of e_0 and e_f from the data obtained in 2005 and in 2008–2010. In agreement with Spitale and Porco (2010), we find that the amplitude of the free mode (ae_f) is slightly greater than that of the forced mode (ae_0), leading to the conclusion that the resonant angle ϕ_2 is indeed likely to be circulating rather than librating. This result applies to all of the models in Table 2. For our adopted fit 6, $ae_f = 36.9 \pm 1.2$ km while $ae_0 = 34.4 \pm 1.4$ km. Fit 5, based on *Cassini* data alone, gives very similar amplitudes of $ae_f = 37.0 \pm 1.2$ km and $ae_0 = 33.4 \pm 1.5$ km. Spitale and Porco (2010) obtained quite compatible values of 37.3 ± 0.4 and 34.6 ± 0.4 km, respectively.

The calculated variations in ae_2 and ϕ_2 over the past three decades, based on our adopted fit, are shown in Fig. 5. As a result of the near-equality of e_f and e_0, the overall amplitude of the $m = 2$ perturbation varies substantially over one complete cycle, from a minimum of $ae_f - ae_0 \simeq 3$ km to a maximum of $ae_f + ae_0 \simeq 71$ km, for fit 6. The period of this variation, $2\pi/\Omega_L \simeq 5.42$ yr, is comparable to the current span of *Cassini* data. Note the extremely rapid motion of ϕ_2 as the amplitude passes through its minimum value, again due to the near-equality of e_f and e_0. Geometrically, our result implies that the short axis of the $m = 2$ perturbation circulates slowly but continuously in a counterclockwise direction (because Ω_L is positive) relative to Mimas, with the amplitude being largest when either of the two radial minima is aligned with Mimas (i.e., at $\phi_2 = 0$) and smallest when either of the maxima is aligned with Mimas (i.e., at $\phi_2 = 180^\circ$).

Prior to *Cassini*'s arrival in July 2004, minima occurred in mid-2001 and early 1996. The latter almost coincided with the HST occultation observed in Nov 1995. This particular data point thus deserves further discussion. From Table 1 we find that $\lambda - \lambda_M = 65.3^\circ$, while Fig. 5 shows that the $m = 2$ phase was $\phi_2 = 133.3^\circ$. Eq. (3) then implies that this observation fell very close to a minimum of the $m = 2$ pattern, with a predicted radial displacement, $\Delta r_2 \simeq -ae_2$. Similarly evaluating the contributions from the $m = 1$ and $m = 3$ modes, we find that $\Delta r_1 \simeq -21$ km and $\Delta r_3 \simeq +4$ km, so that the predicted overall deviation from the mean radius is $\Delta r = -ae_2 - 17$ km. Since the observed value of $r - a = -9.75$ km, and the typical (rms) residual from our model fit is $\sim$10 km, we conclude that ae_2 was no greater than a few km at this time. This is in agreement with the very small amplitude of the $m = 2$ mode in Fig. 5.[5]

4.2.2. Circulation frequency

Spitale and Porco (2010) obtained a value of $\Omega_L = 2(\Omega_2 - n_M) = 0.1792 \pm 0.0014^\circ\ \mathrm{d}^{-1}$ from the *Cassini* imaging data. The constraints

---

[5] In the interest of full disclosure, we note that, since this observation was made only a few months after the Earth ring plane crossing in August 1995, its geometry is very sensitive even to small errors in the direction of Saturn's pole. In addition, the unusually high projected radial velocity of the star across the rings means that small timing errors can translate into comparatively large radial errors.

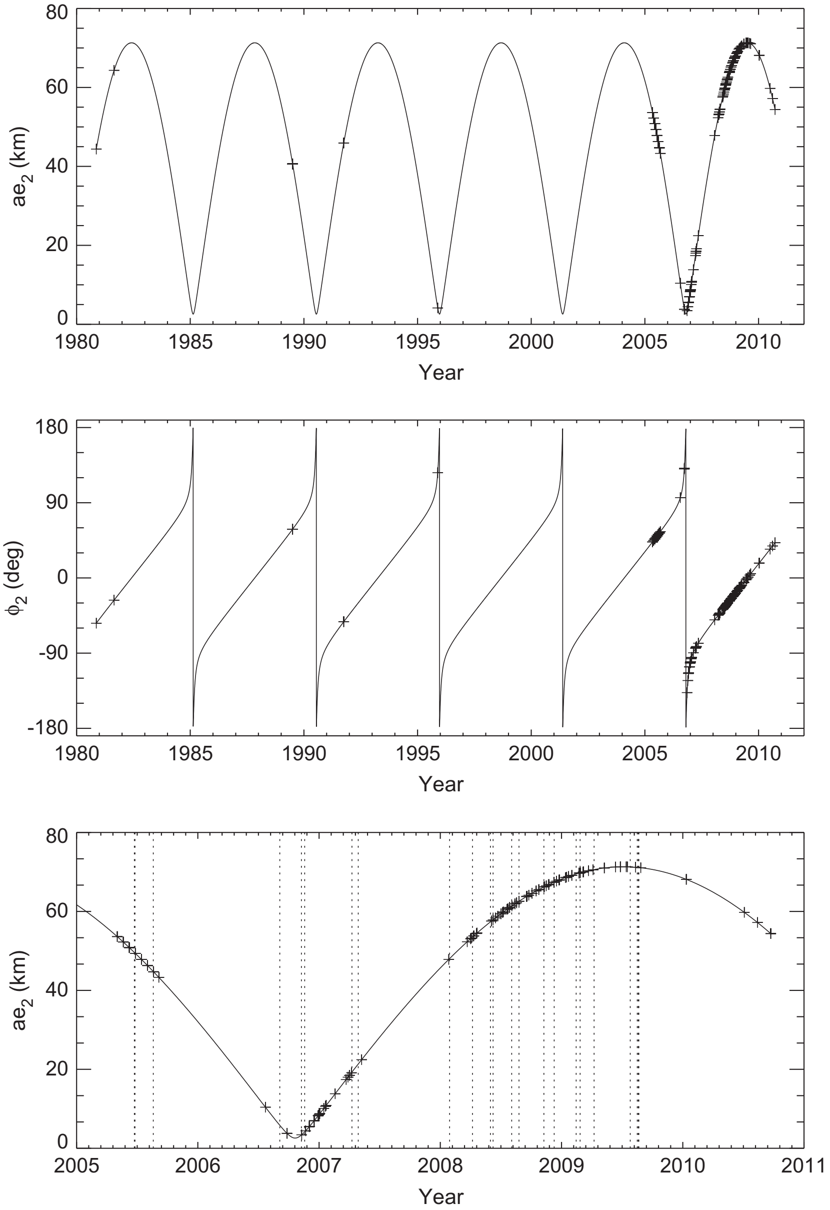

Fig. 5. The model variation in amplitude ae_2 (top panel) and phase ϕ_2 (middle panel) of the $m = 2$ mode over the 28 yr span of occultation observations, for the parameters of fit 6. Crosses indicate the dates of individual observations: *Voyager* 1 and 2 in 1980/1981, 28 Sgr in 1989, the two HST occultations in 1991 and 1995, and finally the much more numerous *Cassini* observations in 2005 (chiefly RSS), 2006/2007 and 2008/2009 (chiefly UVIS and VIMS). In the lower panel, we show the period of *Cassini* observations in greater detail, with vertical dashed lines indicating the times at which imaging observations were obtained (Spitale and Porco, 2010). Amplitude minima occur every 5.42 yr, with the most recent in these data occuring in late 2006.

on the circulation frequency imposed by various subsets of the occultation data are shown most clearly in Fig. 6, where we plot the rms residual as a function of the assumed value of Ω_L. (For each value of Ω_L, we adjusted the other 10 parameters to give the best fit to the data.) With only *Cassini* data included in the fit, there is a single broad minimum in the rms residuals near 0.18° d^{-1}, compatible with Spitale and Porco (2010). If, on the other hand, only the pre-*Cassini* data are fitted, we find multiple narrow minima at $\Omega_L \simeq 0.07$, 0.122, 0.182 and 0.245° d^{-1}, with that at 0.182° d^{-1} being the deepest. These results reflect the densely-sampled but limited temporal coverage of the *Cassini* data, on the one hand, compared with the much sparser distribution of pre-*Cassini* data spanning a much longer interval of time on the other. The latter leads to more precise frequency estimates but also permits ambiguity due to aliasing.[6] The combined fit (shown in the lower panel of Fig. 6) combines the best attributes of both datasets, revealing a single, well-defined minimum at 0.1819 ± 0.0012° d^{-1}.

Finally, we note that although our best-fit solution has e_f slightly greater than e_0 and thus implies that the resonant angle ϕ_2 is circulating, our full suite of fits show that this is the case only for $\Omega_L > 0.175°\ \mathrm{d}^{-1}$. Fig. 7 shows the best-fitting forced and free amplitudes, ae_0 and ae_f and their difference, which is seen to be strongly correlated with the assumed value of Ω_L. If the best-fitting frequency had been even a little less than 0.175° d^{-1}, then we

---

[6] We note in passing that the estimates for Ω_L made by Hedman et al. (2010a) of 0.058 or 0.117° d^{-1}, which also included the *Voyager*, 28 Sgr and 1991 HST data as well as *Cassini* VIMS and RSS data, roughly correspond to two of the secondary minima in Fig. 6.

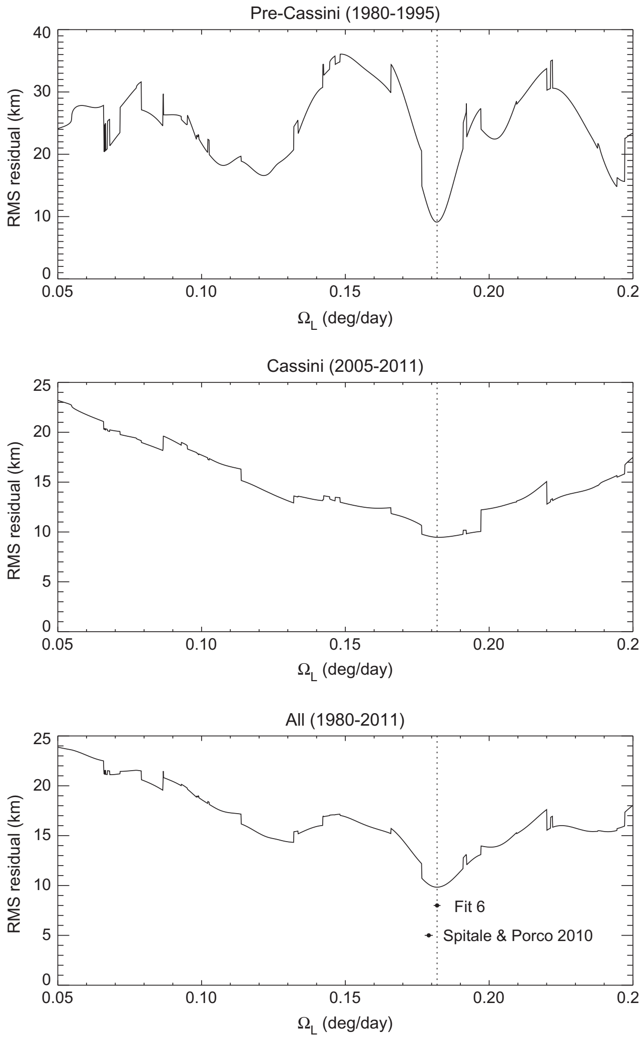

Fig. 6. RMS radial residuals for the B ring edge, plotted as functions of the assumed $m = 2$ libration frequency Ω_L for several different subsets of occultation data. The upper two panels show fits to the pre-*Cassini* data alone, and to the *Cassini* data alone, while the bottom panel shows the fit to the entire data set. The vertical dotted line indicates our best-fitting libration frequency of $0.182 \pm 0.001°\,\mathrm{d}^{-1}$, from fit 6, while the filled circle with error bars indicates the result of Spitale and Porco (2010). The jagged nature of the curves results from the complex shape of the chi-squared hypersurface, as illustrated in Figs. 9 and 11.

might have concluded that $e_0 > e_f$ and that the best-fitting solution implied libration rather than circulation. In other words, it is the tightness of the bound on Ω_L from our fit 6 that enables us to conclude that the $m = 2$ mode is circulating rather than librating.

4.3. The m = 1 pattern

At the mean radius of the B ring edge, $a = 117570.1$ km, the predicted $m = 1$ pattern speed, $\Omega_1 = \dot{\varpi}_{\mathrm{sec}} = 5.0591°\,\mathrm{d}^{-1}$. Our best *Cassini*-only model (fit 5) gives $\Omega_1 = 5.071 \pm 0.007°\,\mathrm{d}^{-1}$, with an amplitude, $ae_1 = 20.7 \pm 1.2$ km (see Table 3 above). Including pre-*Cassini* data (fit 6) yields an almost-identical amplitude, but a significantly faster rate of $5.0835 \pm 0.0016°\,\mathrm{d}^{-1}$. The error bars of the two rates do not overlap, at least at the 1σ level, and both are noticeably slower than the $m = 1$ pattern speed found by Spitale and Porco (2010) of $5.098 \pm 0.003°\,\mathrm{d}^{-1}$. The $m = 1$ pattern rotates $\sim$5 times per year, and has completed $\sim$139 rotations in the 27.0 yr between the *Voyager* and *Cassini* epochs. If we extrapolate fit 5 back to 1981, the 1σ uncertainty in the pericenter longitude is $\sigma(\Omega_1)\Delta t = \pm 70°$. There is thus a distinct possibility of multiple solutions, for which there are one or more additional (or fewer) pericenter rotations over this interval.

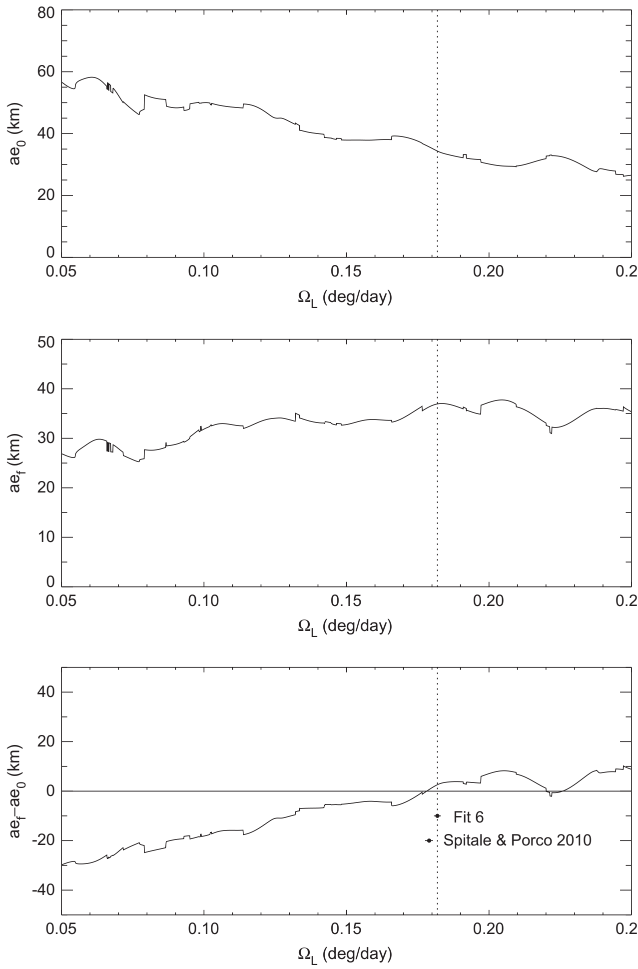

Fig. 7. Variation in the fitted forced and free amplitudes of the $m = 2$ mode as a function of the assumed libration frequency, Ω_L, and of their difference. The vertical dotted line indicates the best-fit value of $\Omega_L = 0.182 \pm 0.001°\,\mathrm{d}^{-1}$, from fit 6, while the filled circle with error bars indicates the result of Spitale and Porco (2010). Note that $e_f > e_0$, implying that the phase angle ϕ_2 circulates, only for $\Omega_L > 0.175°\,\mathrm{d}^{-1}$.

In order to gain more insight into the constraints on Ω_1 imposed by the uneven and sparse temporal distribution of occultation data, we have developed an independent "spectral scanning" program. This procedure takes the residuals from the best-fitting $m = 2$ model fit to the data (equivalent to fit 2 in Table 2), and fits these with a single-mode model for a specified value of m and a range of assumed values of Ω_m. For each value of Ω_m, the best-fitting amplitude, phase and rms residual are recorded and plotted. The results for $m = 1$ are shown in Fig. 8, for the range $4 \leqslant \Omega_1 \leq 6°\,\mathrm{d}^{-1}$. As expected, there is a strong peak in the fitted amplitude near $5.07°\,\mathrm{d}^{-1}$, with a corresponding sharp decrease in the rms residuals from 20 km to $\sim$14 km. However, closer inspection of this figure shows that the central peak is in fact split into two almost equal components, corresponding to $\Omega_1 = 5.053°\,\mathrm{d}^{-1}$ and $5.082°\,\mathrm{d}^{-1}$, with subsidiary maxima at intervals of $\sim 0.027°\,\mathrm{d}^{-1}$, or one extra rotation in 36.5 yr. The double peak suggests that there are two almost equally-good fits that differ by approximately one additional precessional cycle between the *Voyager* and *Cassini* epochs.

However, Fig. 8 provides only a 1-dimensional slice through what is a complex, multi-dimensional phase space. In particular, we anticipate that the $m = 1$ and $m = 2$ pattern speeds are likely

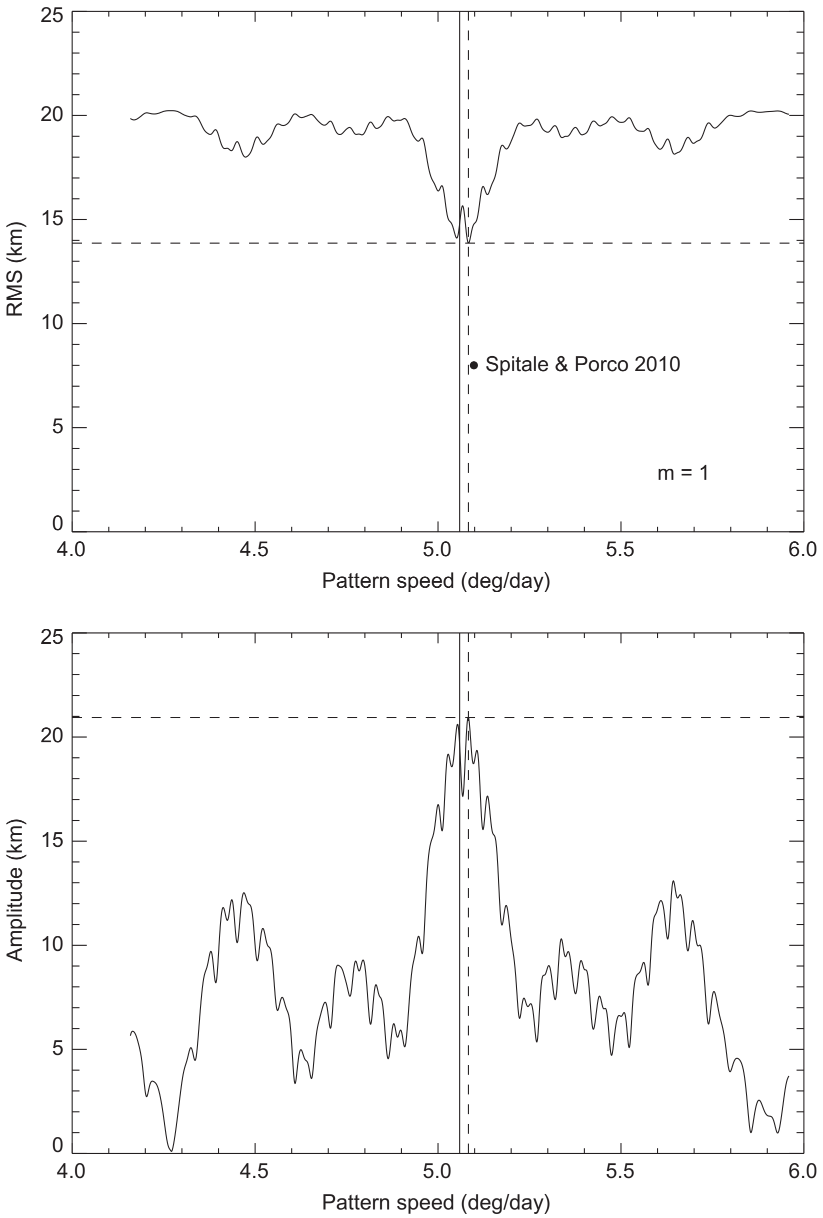

Fig. 8. Normal mode scan for $m = 1$, using the full set of occultation observations, after removal of the $m = 2$ mode. For each assumed value of Ω_1, the amplitude ae_1 and phase δ_1 are adjusted to give the best fit to the data. The solid vertical line marks the predicted pattern speed for the $m = 1$ mode, while the dashed vertical line marks the pattern speed giving the minimum residuals. This is very close to that found by Spitale and Porco (2010), as labeled in the upper panel. Horizontal dashed lines mark the minimum residual (upper panel) and the corresponding peak amplitude (lower panel). Note the double minima in the residuals near the predicted rate.

to be strongly correlated, with adjustments in one being compensated, to some degree, by adjustments in the other. This is illustrated in Fig. 9, where the rms residual is plotted as a function of Ω_L and Ω_1. (At each point in this diagram, the remaining 9 fit parameters have been separately optimized.) The vertical “valley” shows the strong preference for values of Ω_L near 0.182° d^{-1}, but the double minima at $\Omega_1 = 5.053$ and 5.082° d^{-1} are clearly visible. In fact, the chain of white dots, which show the location of the deepest minimum for each value of Ω_L, hops from one of these minima to the other at ~0.185° d^{-1}. We conclude that, with the present data, either of these two solutions for Ω_1 is equally acceptable. The lower value is closer to the calculated apsidal precession rate at the edge of the B ring, but the higher value is a marginally better fit (and thus preferred by our least-squares solution in Table 4) and is closer to (though still significantly less than) the $m = 1$ pattern speed derived by Spitale and Porco (2010).

Finally, we note the prominent sidelobes in Fig. 8 at 4.47 and 5.65° d^{-1}, or ±0.59° d^{-1} with respect to the main peak. These same sidelobes appear if only the *Cassini* data are included in the spectral scan, and we believe that they are due to aliasing of the main peak, rather than to additional $m = 1$ perturbations. More specifically, we suspect they arise because of the two 9-month-long gaps in the *Cassini* data in 2005/2006 and in 2007, shown in Fig. 5. We have confirmed their artificial nature by verifying that they disappear completely when we redo the spectral scan after subtracting the best-fitting $m = 1$ model from the data.

4.4. The m = 3 pattern

At the mean radius of the B ring edge, the predicted $m = 3$ pattern speed $\Omega_3 = (2n + \dot{\varpi}_{\mathrm{sec}})/3 = 507.5319^\circ\ \mathrm{d}^{-1}$. Our best *Cassini*-only model (fit 5) gives $\Omega_3 = 507.700 \pm 0.004^\circ\ \mathrm{d}^{-1}$, with an

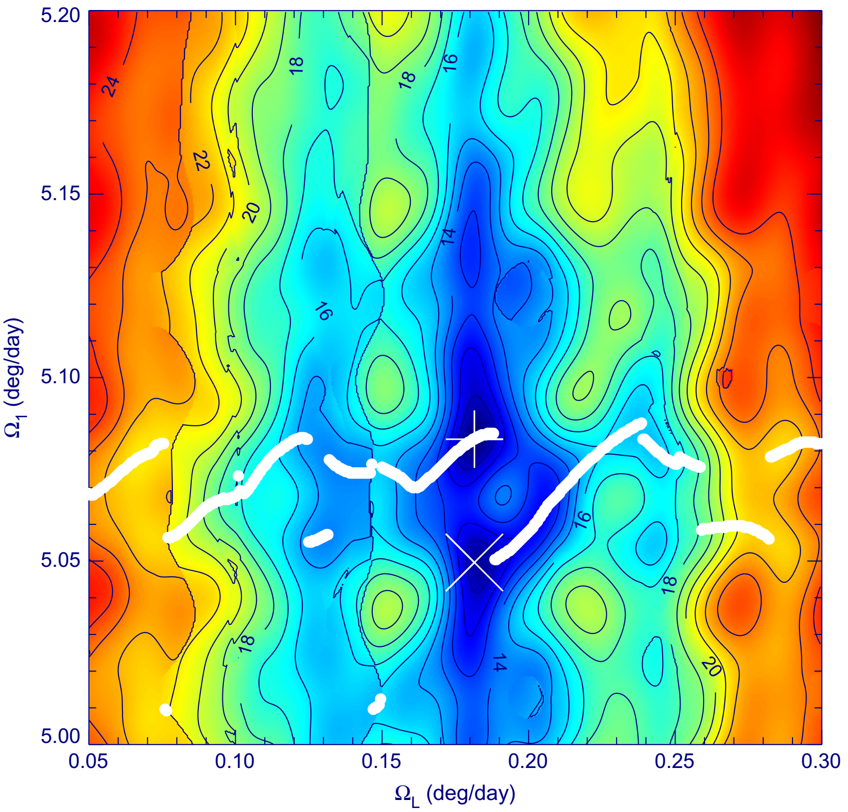

Fig. 9. Contour plot of the post-fit rms residual σ as a function of Ω_L and Ω_1. The blue color indicates the lowest residuals and red the highest. White dots denote the value of Ω_1 that yields the minimum σ for each assumed value of Ω_L. The best overall fit is for $\Omega_L = 0.1819°\ \mathrm{d}^{-1}$ and $\Omega_1 = 5.0835°\ \mathrm{d}^{-1}$ (marked by a +symbol), with $\sigma = 9.8$ km. but an almost equally-deep minimum occurs at $\Omega_1 = 5.053°\ \mathrm{d}^{-1}$ (marked by an $\times$), as seen in Fig. 8. Discontinuities in the white curve are due to the best-fit solution “hopping” between multiple minima in phase space (see text).

amplitude, $ae_3 = 12.9 \pm 1.3$ km (see Table 3 above). Including pre-*Cassini* data (fit 6) results in a slightly faster rate of $507.7027 \pm 0.0014°\ \mathrm{d}^{-1}$, with a slightly-larger amplitude of 13.3 ± 1.2 km. In this case the error bars do overlap, and our results are also quite compatible with that of Spitale and Porco (2010): $\Omega_3 = 507.700 \pm 0.001°\ \mathrm{d}^{-1}$. As in the $m = 1$ case, however, there is a concern that multiple solutions may exist. Extrapolating fit 5 back to 1981, the 1σ uncertainty in the $m = 3$ phase is $3\sigma(\Omega_3)\Delta t = \pm 112°$.

So once again we employ our spectral-scanning program to further explore the constraints on the pattern speed Ω_3. In this case, we take the residuals from the best-fitting $m = 1$ and $m = 2$ model fit to the data and fit these with a single $m = 3$ mode for a range of values of Ω_3. The results are shown in Fig. 10, for the range $506 \leqslant \Omega_3 \leq 509°\ \mathrm{d}^{-1}$. In this case there is a single strong peak in the fitted amplitude at $507.701°\ \mathrm{d}^{-1}$, flanked by weaker subsidiary maxima. The rms residuals decrease from 13.5 km to ~10 km. The mean interval between the subsidiary maxima is $0.017°\ \mathrm{d}^{-1}$, corresponding to one extra rotation in 58 yr, or a single lobe of the $m = 3$ pattern in 19 yr.

As in the $m = 1$ case, we anticipate that the $m = 3$ and $m = 2$ pattern speeds are likely to be strongly correlated and we explore this 2-dimensional slice of phase space in Fig. 11, where the rms residual is plotted as a function of Ω_L and Ω_3. (As in Fig. 9, the remaining 9 fit parameters have been separately optimized.) Again there is a vertical “valley” where $\Omega_L \simeq 0.182°\ \mathrm{d}^{-1}$, which in this case harbors a series of minima in Ω_3 at intervals of $\sim 0.017°\ \mathrm{d}^{-1}$. As above, the chain of white dots shows the location of the deepest minimum for each value of Ω_L, but here there is single well-defined optimal solution at $\Omega_3 = 507.7027°\ \mathrm{d}^{-1}$, in agreement with the least-squares solution in Table 4.

As in Fig. 8, we note the presence in Fig. 10 of prominent sidelobes, in this case at 507.51 and $507.90°\ \mathrm{d}^{-1}$, or $\pm 0.19°\ \mathrm{d}^{-1}$ with respect to the main peak. Again, these same sidelobes appear if only the *Cassini* data are included in the spectral scan, but they disappear completely when we redo the spectral scan after subtracting the best-fitting $m = 3$ model from the data. Note that $0.59°\ \mathrm{d}^{-1} \approx 3 \times 0.19°\ \mathrm{d}^{-1}$, suggesting that the sidelobes in both scans have the same underlying cause, involving one extra cycle of each perturbation in ~600 days. Based on this evidence, we conclude that they are due to aliasing of the main peak, rather than to additional $m = 3$ perturbations.

4.5. Additional modes

Given the existence of unforced $m = 1$ and $m = 3$ normal modes at the edge of the B ring, in addition to the $m = 2$ perturbation driven by the Mimas 2:1 resonance, and the almost 10 km rms residual for even our best 3-mode model (Table 4), it seems not unreasonable to search for further, lower-amplitude modes. Fortunately, our spectral-scanning program is well-adapted for this task, but the potential for multiple solutions grows worse as the value of m increases, partly because the pattern speed increases but mostly because of the narrower spacing of the pattern’s lobes. As an example, for $m = 6$ a difference of only $0.006°\ \mathrm{d}^{-1}$ results in a rotation of one additional lobe in 27 yrs. For this reason, we have attempted to fit these higher-m modes only to the shorter span of densely-sampled *Cassini* data (2005–2010), where such ambiguities are unlikely. Starting with the residuals from the best-fitting model including perturbations for $m = 1$, 2 and 3 (i.e., fit 5 in Table 2), we carried out searches for normal modes for $m = 4$, 5, 6, 7 and

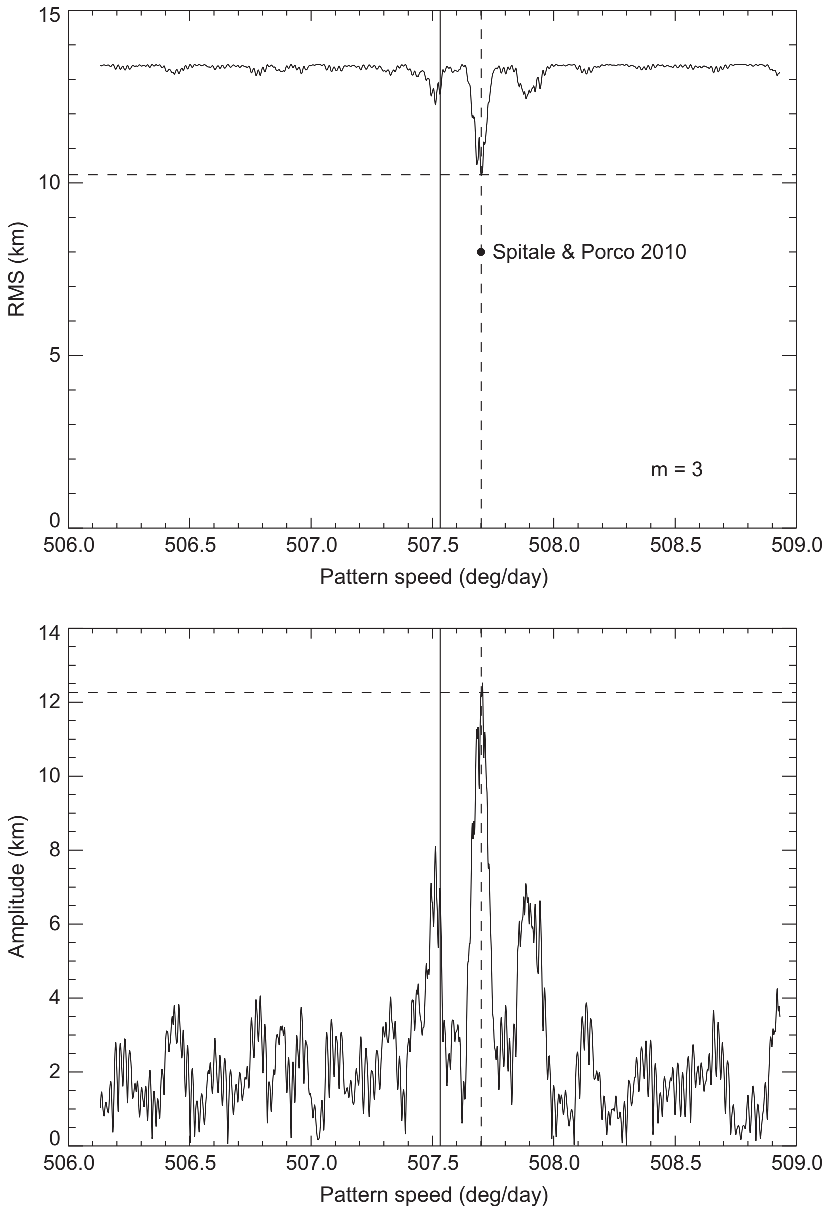

Fig. 10. Normal mode scan for $m = 3$, using the full set of occultation observations, after removal of the $m = 1$ and $m = 2$ modes. For each assumed value of Ω_3, the amplitude ae_3 and phase δ_3 are adjusted to give the best fit to the data. The solid vertical line marks the predicted pattern speed for the $m = 3$ mode, while the dashed vertical line marks the pattern speed giving the minimum residuals. This is again very similar to that found by Spitale and Porco (2010), as labeled in the upper panel. Horizontal dashed lines mark the minimum residual (upper panel) and the corresponding peak amplitude (lower panel).

8, with pattern speeds within ±20° d^{-1} of those predicted by Eq. (10). Evidence for at least two additional normal modes was found, as detailed below.

4.5.1. $m = 4$

At $a = 117570.1$ km, an $m = 4$ normal mode has a predicted pattern speed, $\Omega_4 = (3n + \dot{\varpi}_{\rm sec})/4 = 570.3410^\circ\ \mathrm{d}^{-1}$. A search within a range of ±20° d^{-1} centered on this value revealed a set of four regularly-spaced peaks at frequencies between 570.37 and 570.83° d^{-1}, as shown in Fig. 12. The second peak is slightly higher than the others, with an amplitude of 5.8 km and an rms residual of 8.3 km. The minimum rms residual occurs for $\Omega_4 = 570.509^\circ\ \mathrm{d}^{-1}$. There are no other peaks of comparable height, and only three higher than 5.0 km, between 550 and 590° d^{-1}.

4.5.2. $m = 5$

For $m = 5$, the predicted pattern speed $\Omega_5 = (4n + \dot{\varpi}_{\rm sec})/5 = 608.0264^\circ\ \mathrm{d}^{-1}$, again at $a = 117570.1$ km. A similar search centered on this value, after removing the perturbations for $m = 1, 2, 3$ and 4, shows a pair of significant peaks at frequencies of 608.20 and 608.32° d^{-1}, as shown in Fig. 13. The first peak is higher than the other, with an amplitude of 5.0 km. The minimum rms residual of $\sim$7.3 km occurs for $\Omega_5 = 608.198^\circ\ \mathrm{d}^{-1}$. There are no other peaks of comparable height, and only four in all higher than 4 km, between 588 and 628° d^{-1}.

4.5.3. Searches for other modes

Similar searches for $m = 0$, 6, 7 and 8 did not turn up any additional convincing mode candidates. While peaks with amplitudes in the 4–5 km range are common, the highest of these typically differs by 5–10° d^{-1} from the predicted frequency, whereas those for $m = 4$ and $m = 5$ both fall within 0.2° d^{-1} of the expected value.

Based on the above results, we modified our least-squares fitting program to include normal modes for $m = 4$ and 5, as well as the previous $m = 1$, 2 and 3 perturbations. For each additional

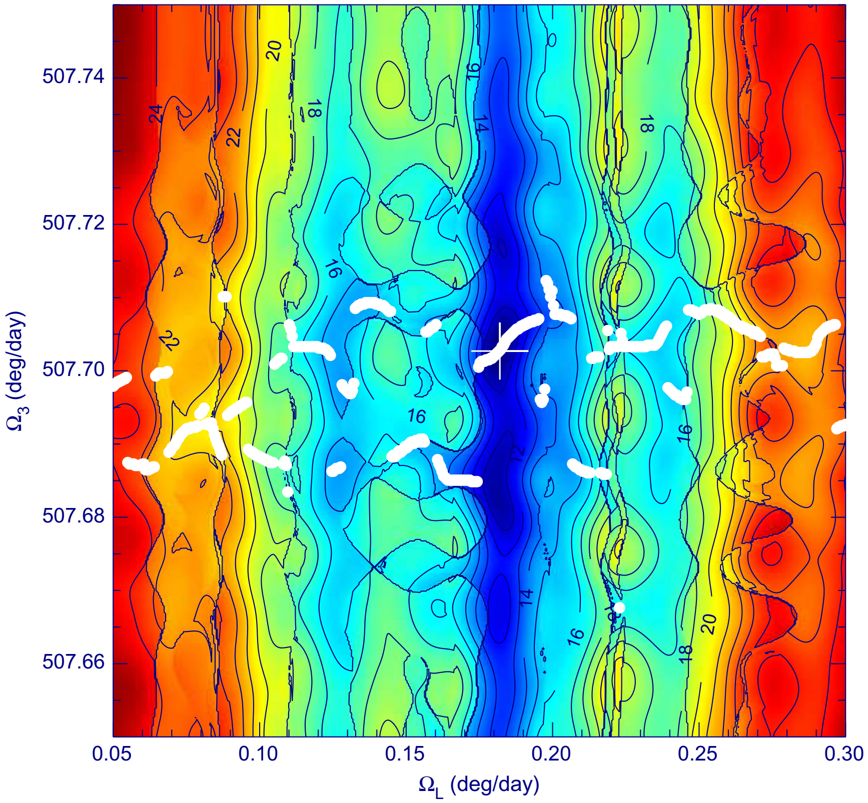

Fig. 11. Contour plot of the post-fit rms residual σ as a function of Ω_L and Ω_3. Blue color indicates the lowest residuals and red the highest. White dots denote the value of Ω_3 that yields the minimum σ for each assumed value of Ω_L. The best overall fit is for $\Omega_L = 0.1819° \mathrm{d}^{-1}$ and $\Omega_3 = 507.7027° \mathrm{d}^{-1}$, marked by a +symbol, with $\sigma = 9.8$ km. Discontinuities in the white curve are due to the best-fit solution "hopping" between multiple minima in phase space (see text).

mode, we fit for 3 parameters: the amplitude, pattern speed and phase at epoch, using the spectral-scan values as *a priori* estimates. As noted above, for these fits we use only the *Cassini* data, due to the high probability of aliasing in any fit extending over a decade or more for these high-order patterns. A complete set of parameters for the best-fitting 5-mode model (fit 11) is listed in Table 5, which may be compared with those for our *Cassini*-only 3-mode model in Table 3. Fitted amplitudes are 5.9 ± 1.0 km for $m = 4$ and 5.6 ± 1.0 km for $m = 5$. The derived pattern speeds are consistent with those found from the spectral scans: $\Omega_4 = 570.509 \pm 0.006° \mathrm{d}^{-1}$ and $\Omega_5 = 608.198 \pm 0.005° \mathrm{d}^{-1}$, where the quoted uncertainties are 1σ formal errors from the nonlinear least-squares fit. The total number of free parameters in this fit is 17 with 133 data points. The overall rms residual is reduced from 9.7 to 7.8 km. All other fitted parameters are consistent with those obtained in fit 5.

4.6. Deviations from the model

In searching for an explanation for the stubbornly large rms residuals for our fits, when compared to the *a priori* measurement and astrometric uncertainties of 1 km or less, it is informative to sort the individual residuals in order of size (without regard to sign) and compare the resulting distribution with that expected for Gaussian noise. We do this in Fig. 14, using a variant of fit 11 in Table 5 for our model that provides the required point-by-point residuals. While the overall rms deviation is 7.3 km, comparable to that in Table 5, the actual distribution of residuals deviates significantly from that expected for Gaussian noise with this value of σ. It is, instead, much better fit by a combination of two separate Gaussian distributions, one with $\sigma_1 = 4.7$ km and the other with $\sigma_2 = 11.2$ km. Approximately 27% of the data fall in the second group. One possible interpretation is that ~70% of the data fall in a "normal" group whose radii lie within ~5 km of the mean ring model, while the remaining 30% scatter over a region about twice as wide.

In their analysis of *Cassini* imaging data, Spitale and Porco (2010) identified two localized regions at the edge of the B ring, denoted A and B, where particularly large deviations (20–30 km) from their own best-fit model occurred. These also correspond to disturbed regions in high-resolution images, and region A showed evidence for vertical (i.e., out of plane) displacements in images taken near the saturnian equinox in August 2009. Spitale and Porco (2010) speculate that these regions, which appeared to move at or near the local Keplerian rate, are the site of large bodies embedded in the rings. In their published orbit models, they excluded regions within ~15° of either putative object. The radial excursions they observed near region A are both local maxima and minima, suggesting that the feature involves eccentricity changes and not only variations in semi-major axis.

We have used the orbital elements given by Spitale and Porco (2010)[7] to predict the locations of regions A and B at the time of each of our occultations, in order to see if the data points that show unusually-large residuals in Fig. 3 can also be linked to these regions. Fig. 15 shows that there is indeed a strong correlation between occultation points that deviate substantially from our best-fitting model and proximity to region A. On the other hand, we see no obvious link to region B in our data.

Concentrating on region A, therefore, we note that 13 of the 16 data points with residuals greater than 15 km lie within ±45° of its published ephemeris. These include the largest two individual residuals of ~31 km, corresponding to the UVIS ϵ Cen (65) and

---

[7] Note that the published elements are incorrect; we are grateful to J. Spitale (personal communication) for providing the following values that match the J2000 longitudes in Spitale and Porco (2010): region A: epoch 2008-264T01:57:03.343, longitude 110 ± 1°; region B: epoch 2007-091T07:26:27.231, longitude 141 ± 2°.

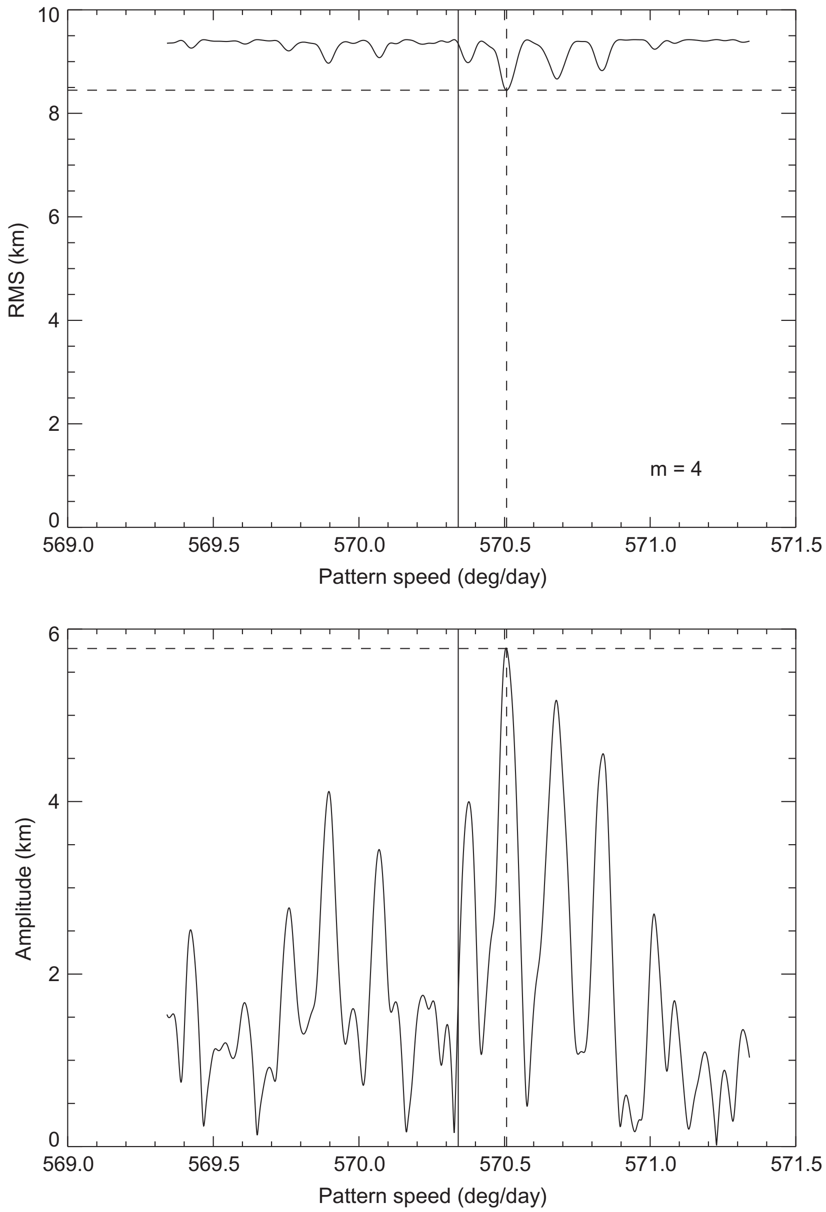

Fig. 12. Normal mode scan for $m = 4$, using the *Cassini* occultation data only, after removal of the $m = 1$, 2 and 3 modes. For each assumed value of Ω_4, the amplitude and phase are adjusted to give the best fit to the data. The solid vertical line marks the predicted pattern speed for the $m = 4$ mode; the dashed vertical line marks the pattern speed giving the minimum residuals. Horizontal lines mark the minimum residual (upper panel) and the corresponding peak amplitude (lower panel).

VIMS γ Cru (101) events. We also note that none of these offending measurements comes from noisy data, or is otherwise suspect, and that, on the contrary, several involve occultations of α Leo, α Sco, and γ Cru, which are among the brightest stars observed by *Cassini* in the UV and near-IR. We thus conclude that all of these large residuals are likely to represent real deviations from our analytical model, and that most are associated with whatever local perturbation gives rise to region A.

When the influence of region A is removed, as shown in the lower panel of Fig. 15 the remaining residuals appear to be randomly distributed relative to region B.

5. Graphical model

Although least-squares fits enable us to estimate the optimal values of the model parameters, we have also made an attempt to visualize directly the perturbation of the B ring edge associated with the Mimas 2:1 resonance. Ideally, we would like to estimate the amplitude e_2 and phase ϕ_2 of the $m = 2$ mode as a function of time, for direct comparison with the predicted motion shown in Fig. 1. This is relatively straightforward to do with imaging data, where the entire ring edge is seen over a period of only a few hours, but more difficult to do with occultation data, which are typically distributed over many months or even years. We can, however, make use of the fact that the resonant libration is quite slow to construct "snapshots" of the ring edge at different times during the *Cassini* mission.

We start with Eq. (3), which we rewrite in more compact form as

$$\Delta r \approx -ae_2 \cos(2\Delta\lambda - \phi_2) \tag{14}$$

where $\Delta r = r(\lambda,t) - a$ and $\Delta\lambda = \lambda - \lambda_M$. Expanding the trig function and again introducing the variables $h = e_2 \cos \phi_2$ and $k = e_2 \sin \phi_2$ as in Fig. 1, we have

$$\Delta r = -ah \cos(2\Delta\lambda) - ak \sin(2\Delta\lambda). \tag{15}$$

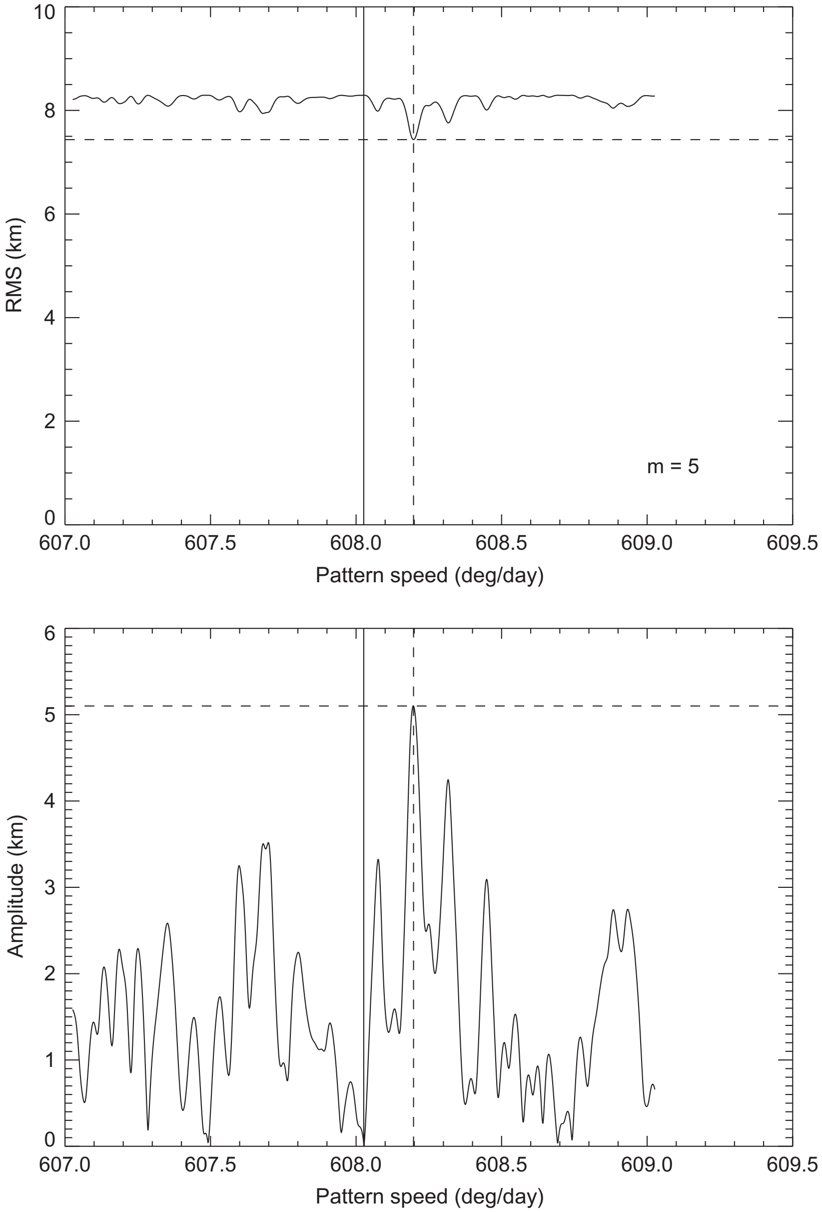

Fig. 13. Normal mode scan for $m = 5$, using the *Cassini* occultation data only, after removal of the $m = 1$, 2, 3 and 4 modes. For each assumed value of Ω_5, the amplitude and phase are adjusted to give the best fit to the data. The solid vertical line marks the predicted pattern speed for the $m = 5$ mode; the dashed vertical line marks the pattern speed giving the minimum residuals. Horizontal lines mark the minimum residual (upper panel) and the corresponding peak amplitude (lower panel).

For any given ring observation, we have r and λ at a known time, t. We can also calculate λ_M, the mean longitude of Mimas at t, and thus $\Delta\lambda$. With an *a priori* value of the mean radius, a, we can calculate Δr. Eq. (15) then provides a linear relation between the unknown and slowly-varying libration parameters h and k. The slope of this line in (h,k) space is $dk/dh = -\cot(\Delta\lambda)$ and its perpendicular distance from the origin is $p = |\Delta r|/a$.

Since h and k are expected to vary slowly with time, multiple occultations separated by up to a few months should thus yield a series of straight lines in (h,k) space, intersecting at a point that specifies the actual value of (h,k), or equivalently (e_2, ϕ_2), at that time. A limitation to this approach, in addition to measurement errors in Δr, lies in unmodeled variations in r; in particular, the radial perturbations associated with the $m = 1$ and $m = 3$ normal modes, which can each contribute as much as 10–20 km to the scatter in Δr.

We can apply this method to illustrate the variation in e_2 and ϕ_2 during the period of the *Cassini* mission by breaking the occultation data into six subsets, each corresponding to a period of 3–6 months, as shown in Fig. 16. In each panel, we plot the straight lines corresponding to the various occultations, color-coded by orbit number. The black circle illustrates the predicted variation in h and k according to Eqs. (5) and (6), using the best-fit parameters derived above (see Table 3), and the color-coded symbols on the circle indicate the predicted (h,k) values on each date. The phase clearly starts at $\phi_2 \sim 50°$ in mid-2005, with an amplitude of $ae_2 \sim 50$ km, as also seen in the top panel of Fig. 2. The amplitude reaches a minimum in 2006/2007 and ϕ_2 becomes indeterminate as the indicated value of (h,k) passes very near the origin. By early 2008, ϕ_2 has increased to $\sim$320° and ae_2 is again $\sim$50 km. Subsequently, the phase and amplitude both increase more slowly, the phase reaching $\sim$350° and the amplitude a near-maximum value of $\sim$70 km in mid-2009 (cf. the bottom panel of Fig. 2).

Despite the fairly large scatter in our graphical estimates of the $m = 2$ parameters, the full suite of *Cassini* occultation data clearly supports the conclusion that the resonant variable ϕ_2 is circulating

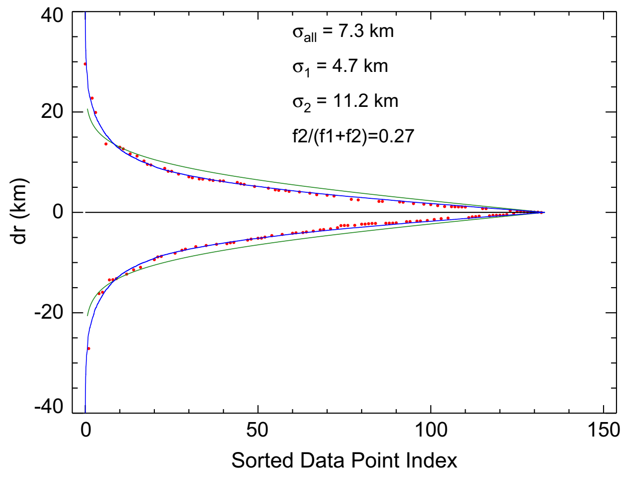

Fig. 14. The distribution of post-fit residuals for the *Cassini* stellar occultation data relative to a best-fitting 5-mode model similar to fit 11 in Table 5. The 133 individual data points are sorted in order of decreasing magnitude of the residual, with point '0' having the largest residual (+29 km). The green curve shows the expected distribution of sorted residuals for a fit with Gaussian noise having $\sigma = 7.3$ km, the standard deviation of the ring plane radius residuals of the 5-mode fit. The observed distribution of residuals deviates significantly from the Gaussian model. The blue curve shows a much better match, based on a two-component Gaussian model in which 73% of the data have $\sigma_1 = 4.7$ km and 27% have $\sigma_2 = 11.2$ km. (For interpretation of the references to color in this figure legend, the reader is referred to the web version of this article.)

in the counter-clockwise direction about a fixed point at $\phi_2 \simeq 0$. The subset of VIMS and RSS observations analyzed by Hedman et al. (2010a) were restricted largely to mid-2005 and 2008, corresponding to the first, third and fourth panels in Fig. 16, from which they concluded erroneously that the phase ϕ_2 had *decreased* from $\sim 70°$ to $\sim 320°$. From Fig. 16, we can see now that the phase was in fact *increasing* through 2008 and 2009, consistent with the counter-clockwise circulation model of Spitale and Porco (2010).

While the occultation data from July 2006 to April 2007, shown in the second panel of Fig. 16 confirm that the amplitude was extremely small, it is impossible to determine the phase at this time with any confidence. It is thus not possible to decide from this figure alone whether the resonant argument is librating about 0° with an amplitude near 90° or circulating in a counterclockwise direction. From Fig. 1, we see that this depends on establishing the value of ϕ_2 when the overall $m = 2$ amplitude is near its minimum value: if $\phi_2 \simeq 0$, then the system is librating, while if $\phi_2 \simeq \pi$, the system is circulating. Spitale and Porco (2010) were able to conclude, on the basis of their analysis of azimuthal imaging profiles obtained during the critical period in late 2006 and early 2007 (see their Fig. 3), that ϕ_2 indeed passed through 180° and so must be circulating. Although our least-squares model fits in Section 4 indirectly support this conclusion, by confirming that $e_f > e_0$, the graphical analysis in Fig. 16 unfortunately shows too much scatter to clearly distinguish circulation from libration.

6. Discussion

6.1. The $m = 2$ perturbation

Although our results confirm the long-held belief that the radial distortion of the outer edge of the B ring is dominated by an $m = 2$ pattern associated with the 2:1 inner Lindblad resonance with Mimas, it is clear that the full story is much more complicated than originally envisioned by Goldreich and Tremaine (1978). In agreement with Spitale and Porco (2010), we find that the $m = 2$ pattern circulates slowly in a prograde direction relative to Mimas. The circulation frequency, based on 28 yrs of occultation data, corresponds to a period of $2\pi/\Omega_L = 5.42$ yr. At the same time, the $m = 2$ amplitude varies from a minimum of ~ 3 km to a maximum of ~ 71 km, because of the near-equality of the forced and free components of the distortion, as illustrated in Figs. 1, 5 and 16. The most recent minimum in the occultation data considered here occurred in late 2006; the subsequent minimum is expected to have occurred in early 2012, unfortunately in a period of near-equatorial orbits and few ring observations. We must thus await future *Cassini* observations to confirm this.

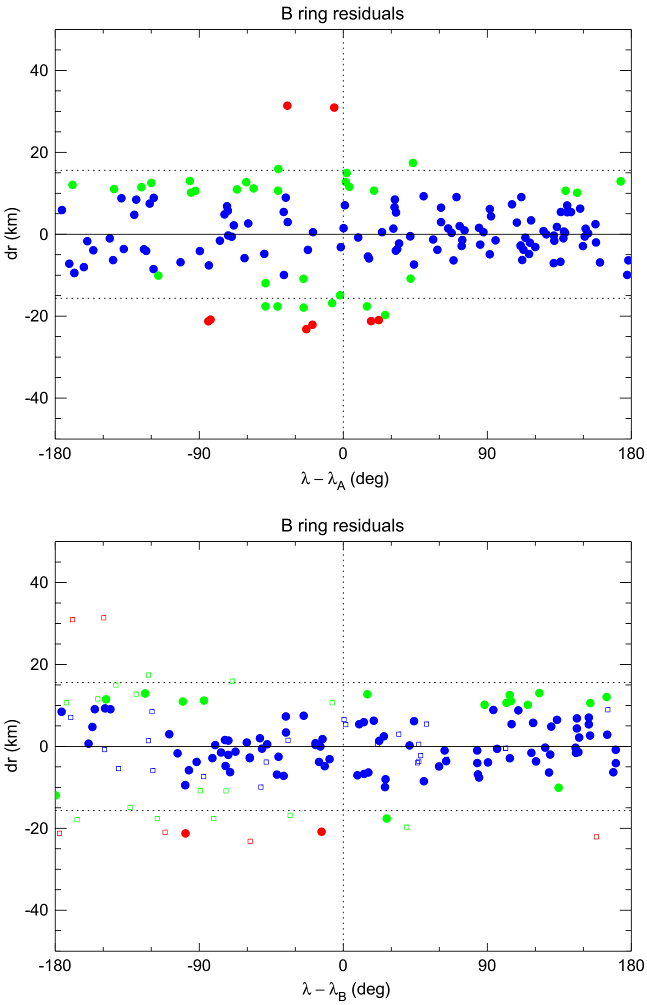

Fig. 15. The distribution of post-fit residuals for the *Cassini* stellar occultation data relative to the best-fitting 5-mode model (fit 11 in Table 5), plotted in a longitude system rotating at close to the Keplerian rate at the outer edge of the B ring. The upper panel shows the longitude relative to region A of Spitale and Porco (2010), while the lower panel shows the longitude relative to region B. Red dots indicate residuals of 20 km or more, green dots residuals between 10 and 20 km, and blue dots residuals less than 10 km; horizontal dotted lines mark the $\pm 2\sigma$ levels. The largest residuals appear to be concentrated near region A. In the lower panel, the data points which fall within 45° of feature A are plotted as small open squares, in order to focus attention on region B.

An equivalent view of this situation is that a free $m = 2$ normal mode coexists at the B ring's edge, superimposed on the forced perturbation by Mimas. From fit 6, the amplitude of the former, $ae_f = 36.9 \pm 1.2$ km, is slightly greater than the forced amplitude of $ae_0 = 34.4 \pm 1.4$ km. Spitale and Porco (2010) obtained very similar results, with $ae_f = 37.3 \pm 0.4$ km and $ae_0 = 34.6 \pm 0.4$ km. The underlying reason for this near-equality of e_0 and e_f is not clear. One possible interpretation is that at some time in the past, the ring edge was circular, and then the Mimas perturbation was

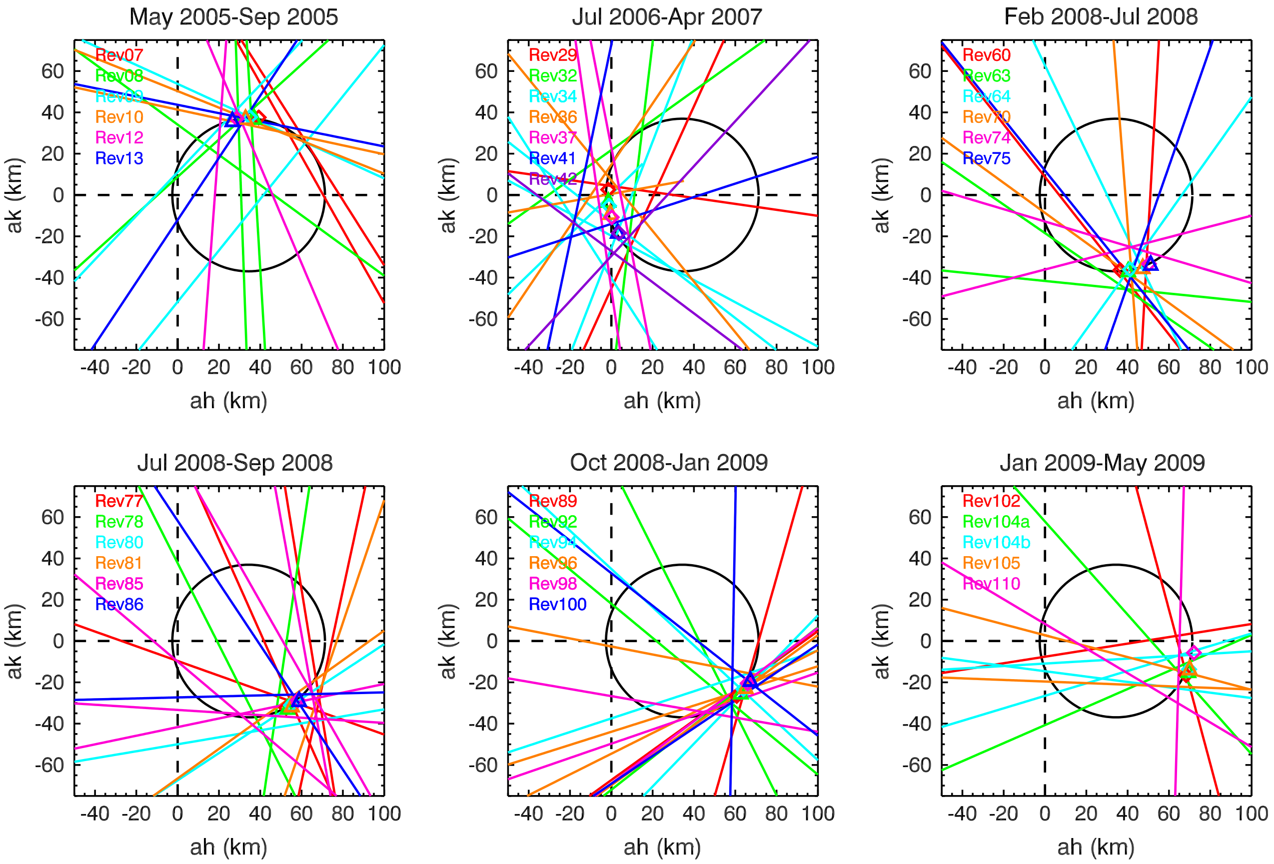

Fig. 16. Graphical determination of parameters for the $m = 2$ perturbation in the *Cassini* data, using the method described in the text. Each panel shows occultation measurements from a three to nine month period, color-coded by orbit number (see key). The black circle illustrates the predicted variation in h and k, using the nominal fit parameters from Table 3. Color-coded symbols 'indicate the predicted (h, k) values for each occultation. The counterclockwise motion is evident, as is the minimum in eccentricity in late 2006 or early 2007. The eccentricity was approaching a maximum in mid-2009. Note the 9-month gaps between panels 1 and 2 and between panels 2 and 3, due to an absence of ring occultations in these periods. Data from the UVIS instrument are not included in this plot.

'turned on' abruptly. But not only is it difficult to imagine such a scenario, we would expect that interparticle collisions would damp the free mode, leaving only the forced perturbation. (However, recent numerical simulations by Hahn and Spitale (2013) suggest that damping may be much less efficient than previously thought, with free modes surviving for at least 10^5 orbits.) A variant on this hypothesis is that the overall $m = 2$ amplitude is periodically "reset" to zero, which would have the effect of reestablishing a free eccentricity equal to e_0. Perhaps more likely is the idea that the forced mode somehow continuously regenerates the free mode, perhaps through nonlinear collisional interactions. Some support for this notion is provided by numerical simulations of the edge of the B ring by Hahn et al. (2009, 2012). In this context, it is possible that both the forced and free modes are subject to a common limitation on their amplitudes associated with viscous dissipation. Several other resonant systems, including the librating small saturnian satellite Aegaeon (Hedman et al., 2010b) and the Encke gap ringlets (Hedman et al., 2013), share this characteristic of equal free and forced amplitudes.

How closely do the characteristics of the forced $m = 2$ mode match those predicted by the idealized test-particle model of Hedman et al. (2010a)? The best-determined parameter is the circulation frequency, $\Omega_L = +0.1819 \pm 0.0012^\circ\ \mathrm{d}^{-1}$, which the model predicts is related to the distance of the test particle from the resonant radius, $a_{\rm res}$. From Eq. (8), the observed value of Ω_L corresponds to $\bar{a} - a_{\rm res} = -18.8 \pm 0.1$ km, where $\bar{a}$ might be thought of as an "effective," or mass-weighted, radius of the perturbed ring material. This is in contrast with the observed mean radius of the B ring edge, $a_B = 117570 \pm 1$ km, which is ~16 km *exterior* to the calculated radius of the Mimas 2:1 ILR, $a_{\rm res} = 117553.7$ km.[8] The conclusion that the effective radius of the perturbed region of the B ring is located interior to the resonant radius is consistent with the observation that the resonant variable ϕ_2 is observed to circulate in a counterclockwise direction about a fixed point at $\phi_2 = 0$, rather than clockwise about $\phi_2 = \pi$, as illustrated in Fig. 1.

According to the test-particle model, the forced amplitude ae_0 is also determined by the distance from exact resonance, via Eq. (7). Using $\bar{a} - a_{\rm res} = -18.8$ km, this expression predicts that $ae_0 = 24$ km. This is comparable to, but rather less than, the observed forced amplitude of 34 km. An alternative approach, as adopted by Spitale and Porco (2010), is to use the observed distance between $a_{\rm res}$ and the actual outer edge of the B ring, $a_B - a_{\rm res} = +14.2$ km, which leads to a forced amplitude of 32 km. But we have just noted above that this should give rise to libration or circulation about $\phi_2 = \pi$, in disagreement with the observations. Moreover, as noted by Hedman et al. (2010a), the classical "width" of the 2:1 resonance is ~43 km, and within this zone we cannot expect the test-particle model to give very reliable quantitative results.

In summary, the actual mean radius of the edge of the B ring is located ~14 km exterior to the Mimas 2:1 ILR, but the ring's observed orientation relative to Mimas, the rate and direction of circulation of the observed $m = 2$ perturbation and its forced

---

[8] Calculated using the long-term mean motion of Mimas. If instead one uses the average mean motion in 2007, $a_{\rm res}$ moves outwards to 117555.8 km (Spitale and Porco, 2010).

amplitude of 34 km are all consistent with the expected behavior of ring particles located ~15 km *interior* to the resonant radius. Following Porco et al. (1984), we may attribute this to the fact that most of the mass of the outer B ring is located interior to the resonance, and to collective effects operating within the ring—both gravitational and collisional—that act to prevent the 180° phase shift in ϕ_2 across the resonance predicted by the simple test-particle model.

6.2. Additional modes

In addition to the circulating and pulsating $m = 2$ distortion, Spitale and Porco (2010) also reported strong evidence for both $m = 1$ and $m = 3$ normal (or free) modes, with amplitudes of 20.9 ± 0.3 km and 11.8 ± 0.3 km, respectively. Our three-mode fit to the full set of occultation data confirms the existence of these perturbations, for which we find very similar mean amplitudes of 20.6 ± 1.2 km and 13.3 ± 1.2 km, respectively, and pattern speeds close to those predicted by Eq. (10). The $m = 1$ mode is equivalent to a freely-precessing Keplerian ellipse, and rotates at a rate approximately 100 times slower than the $m = 2$ and $m = 3$ modes. However, the amplitude of the $m = 3$ mode (and possibly also that of the $m = 1$ mode) appears to have decreased steadily between 2005 and 2009.

Our fits also show good evidence for normal modes with $m = 4$ and $m = 5$, though these are less certain, given their smaller amplitudes of 5–6 km. Additional modes may also exist, probably with even smaller amplitudes.

Spitale and Porco (2010) attribute each free mode seen at the B ring edge—including the free component of the $m = 2$ mode—to excitation of a "resonant cavity" that is bounded by the sharp ring edge and a resonant radius located at some distance interior to the edge. For each value of m, the standing oscillation in this cavity can be thought of as a superposition of inward and outward-propagating density waves with a common pattern speed, Ω_m. The resonant radius, a_{res} is determined by the location where Eq. (10) is satisfied, i.e., where $(m-1)n + \dot{\varpi}_{sec} = m\Omega_m$. The origin of the oscillations is suspected to lie in a viscous overstability, following a suggestion by Borderies et al. (1985).

In this model, the pattern speed of each mode is self-selected such that the distance between a_{res} and the B ring edge a_B is a specific fraction Γ of the radial wavelength of the corresponding density wave λ. Spitale and Porco (2010) test this model by comparing the calculated cavity widths $a_B - a_{res}$ with those predicted by the standard linear density wave theory. Assuming that $\Gamma = 0.5$ or 0.25, they find reasonable agreement with the cavity model for a surface mass density in the outermost B ring of Σ = 40–100 g/cm^{-2}.

Although the original concept of a "resonant cavity" was based on WKB expressions for the density wave dispersion relation given by Goldreich and Tremaine (1979), more recent unpublished numerical calculations (P. Goldreich, personal communication) which use the full wave equation confirm that standing waves can indeed be trapped at a sharp ring edge, and that the disturbance decays exponentially interior to the resonant radius, a_{res}. However these simulations, which employ the nonlinear density wave model of Borderies et al. (1986), also suggest that the above analytic estimates for the surface mass density are probably too low by about a factor of four.

One obvious requirement of this model is that the observed values of Ω_m are slightly *greater* than those predicted by Eq. (10) at $a = a_B$, so that $a_{res} < a_B$. We find that this is indeed true for all of the modes we have convincingly identified. In Table 6 we test the "resonant cavity" model, using our own estimates of Ω_1, Ω_2 and Ω_3 as well as the pattern speeds derived for the putative $m = 4$ and $m = 5$ modes. (Recall from Section 3 that the pattern speed of the free $m = 2$ mode is given by $\Omega_2 = n_M + \Omega_L/2$.) For each normal mode, we list our best-fit value of Ω_m, the calculated resonant radius a_{res} (based on Eq. (10) and the gravity solution of Jacobson (2006), $\Delta a = a_B - a_{res}$ and the implied value of Σ, assuming $\Gamma = 0.25$.

Table 6
Normal mode cavities and B ring surface densities.

Mode m	Ω_m[a] (° d^{-1})	a_{res}[b] (km)	Δa[c] (km)	$\Sigma_{0.25}$[d] (g cm^{-2})
1	5.0807	117438.2	131.9	11.8
2	382.0737[e]	117537.7	32.4	48.1
3	507.6998	117544.3	25.8	60.6
4	570.5088	117547.3	22.8	71.0
5	608.1980	117548.2	21.9	87.0

[a] Fitted pattern speed (see Table 5).
[b] Calculated resonant radius.
[c] Cavity width, based on a mean edge radius of a_B = 117570.1 km.
[d] Ring surface mass density for Γ = 0.25 (see text).
[e] $\Omega_2 = n_M + \Omega_L/2$.

In calculating the required surface density, we depart slightly from Eq. (3) of Spitale and Porco (2010), which was derived by equating the distance Δa to the fractional wavelength $\Gamma\lambda$ with λ evaluated at a_B. But the radial wavenumber, k of a density wave increases linearly with distance from the Lindblad resonance, according to the asymptotic expression (Goldreich and Tremaine, 1978):

$$k(a) \simeq \frac{\mathcal{D}(a - a_{res})}{2\pi G \Sigma a_{res}}, \tag{16}$$

where the parameter $\mathcal{D}$ is given by

$$\mathcal{D} = n^2\left[3(m-1) + \frac{21}{2}J_2(R_p/a_{res})^2\right]. \tag{17}$$

Here, J_2 is the usual zonal gravity coefficient and R_p is the planet's reference radius. Letting $x = a - a_{res}$, we can write an expression for the accumulated phase difference across the wave:

$$\psi(x) = \int_0^x k(x)dx \simeq \frac{\mathcal{D}x^2}{4\pi G \Sigma a_{res}}. \tag{18}$$

Setting $\psi(\Delta a) = 2\pi\Gamma$, and using Kepler's third law to eliminate n in terms of a_{res}, we can solve for the required surface density:

$$\Sigma \simeq \frac{M_p\left[3(m-1) + \frac{21}{2}J_2(R/a)^2\right]\Delta a^2}{8\pi^2\Gamma a_{res}^4}, \tag{19}$$

where M_p is the mass of the planet. This is exactly one-half of the expression given by Spitale and Porco (2010).

Taking $\Gamma = 0.25$, which amounts to placing the first maximum in the standing wave at the gap edge, we find values of Σ for $2 \leqslant m \leqslant 5$ that vary from 48 g cm^{-2} to 87 g cm^{-2}. Allowing for the likely underestimation by this simple calculation of the true surface mass density mentioned above, a more plausible range of densities is 200–350 g cm^{-2}. In fact, fairly good matches to our observed values of a_{res} for $2 \leqslant m \leqslant 5$ are found for Σ = 200 g cm^{-2} (P. Goldreich, personal communication).

There are few independent estimates of the surface density in the outer B ring, due to the paucity of identified density or bending waves, but Lissauer (1985) obtained Σ = 54 g cm^{-2} from an analysis of the Mimas 4:2 bending wave at 116724 km, which lies ~800 km interior to the B ring edge.

However, the calculated resonance location for the $m = 1$ mode gives a much lower, and rather implausible, value for Σ of only 12 g cm^{-2}. The marked discrepancy between this result and that obtained by Spitale and Porco (2010), who obtained a value of at least 44 g cm^{-2} for this mode (and 87 g cm^{-2} for Γ = 0.25) is traceable to their significantly greater value for Ω_1 (see Table 2), which results in a much greater resonant cavity width of $\Delta a \simeq 250$ km. We have not been able to resolve or explain this difference, which is quite surprising given how similar our results are for $m = 2$ and $m = 3$. One might ask if there is direct evidence in the optical depth profiles for a significant $m = 1$ disturbance extending 100 km or more interior to the outer edge of the B ring. The substantial optical depth and complex nature of this region, plus the large $m = 2$ distortion, make such a comparison difficult, but we can address this issue with a sequence of 16 VIMS occultations of the very bright star, γ Crucis, obtained in 2008/2009. With a ring opening angle of 62.35°, these occultations do penetrate at least the outer B ring, and provide a consistent set of profiles at various corotating longitudes. Preliminary analysis of these data shows evidence for significant $m = 1$ perturbations, with a pattern speed near the expected value of $5.08^\circ\ \mathrm{d}^{-1}$, extending at least 400 km inwards from the ring edge. This study will form the subject of a subsequent paper. Movies made from sequences of ISS images of the B ring edge also show evidence for significant radial distortions extending ~250 km inwards from the edge (C. Porco, personal communication).

6.3. Loose ends

Even though the observed $m = 2$ perturbation seems reasonably consistent with our simple resonant model, and the normal mode frequencies are mostly compatible with the resonant cavity picture and plausible surface mass densities, we must not forget that the post-fit rms residuals for our best-fitting model remain stubbornly large, at ~7.7 km, whereas the uncertainties in the individual measurements are estimated at under 1.0 km. This situation is highly unusual, inasmuch as the sharp edges of the narrow uranian ringlets that have been the subject of similar occultation studies are well-fitted by simple models involving one or more such global modes (cf. French et al., 1988, 1991). Indeed, fits to a dozen or so other non-circular features in the C ring and Cassini Division, using the same occultation data set and measurement protocols, yield post-fit residuals of 0.3–1.0 km (French et al., 2011; Nicholson et al., 2011). This despite the fact that for many of the latter features, the location of the edge is much harder to define and measure than it is for the B ring edge. It is thus clear that the large B ring edge residuals represent real, unmodeled distortions, as already noted and illustrated by Spitale and Porco (2010). A possible analog is provided by the edges of the Encke and Keeler gaps, which exhibit remarkably complex radial perturbations due to interactions with the embedded satellites, Pan and Daphnis (Tiscareno et al., 2005; Torrey et al., 2008). However, no such satellite has been identified in the Huygens Gap, and the nearby Huygens ringlet does not show the same obvious distortions as the B ring edge. Spitale and Porco (2010) instead suggest that these large distortions are associated with the presence of several massive bodies embedded within the outer few 10s of km of the B ring. In Fig. 15 we have seen evidence that at least the largest residuals are indeed associated with their "region A." Such localized disturbances are not amenable to modeling in terms of global modes, and may forever doom attempts to predict the radius of the B ring edge to better than ~10 km.

Acknowledgments

We are grateful to Peter Goldreich for several stimulating discussions of the dynamical environment of the B ring, and the nature of "normal modes" in rings, as well as for providing unpublished results from his numerical models. The determination of the absolute radius scale used for this work was based on the measurement of thousands of features in the occultation observations of Saturn's rings, performed over several years by "Team Cassini" leaders Katherine Lonergan, Talia Sepersky, and over two dozen Wellesley College undergraduates. Joe Spitale and a second eviewer provided several insightful comments which led to improvements in our presentation. This work was supported in part by the Cassini Data Analysis Program.

References

Bevington, P.R., Robinson, D.K., 2003. Data Reduction and Error Analysis for the Physical Sciences. McGraw-Hill, Boston, MA, ISBN: 0-07-247227-8.

Borderies, N., Goldreich, P., Tremaine, S., 1985. A granular flow model for dense planetary rings. Icarus 63, 406–420.

Borderies, N., Goldreich, P., Tremaine, S., 1986. Nonlinear density waves in planetary rings. Icarus 68, 522–533.

Bosh, A.S., 1994. Stellar Occultation Studies of Saturn's Rings with the Hubble Space Telescope. Ph.D. Thesis, MIT, Cambridge.

Bosh, A.S., Olkin, C.B., French, R.G., Nicholson, P.D., 2002. Saturn's F ring: Kinematics and particle sizes from stellar occultation studies. Icarus 157, 57–75.

Colwell, J.E., Esposito, L.W., Jerousek, R.G., Sremčević, M., Pettis, D., Bradley, E.T., 2010. Cassini UVIS stellar occultation observations of Saturn's rings. Astron. J. 140, 1569–1578.

Elliot, J.L. et al., 1993. An occultation by Saturn's rings on 1991 October 2–3 observed with the Hubble Space Telescope. Astron. J. 106, 2544–2572.

Esposito, L. et al., 1983. Voyager photopolarimeter stellar occultation of Saturn's rings. J. Geophys. Res. 88, 8643–8649.

Esposito, L.W., Albers, N., Sremčević, M., Meinke, B., Stewart, G. 2009. UVIS observations of B-ring outer edge: Comparisons to F-ring. In: European Planetary Science Congress 2009, p. 694.

French, R.G. et al., 1988. Uranian ring orbits from Earth-based and Voyager occultation observations. Icarus 73, 349–378.

French, R.G. et al., 1993. Geometry of the Saturn system from the 3 July 1989 occultation of 28 SGR and Voyager observations. Icarus 103, 163–214.

French, R.G. et al., 2011. Noncircular features in Saturn's rings: I. The Cassini Division. In: European Planetary Science Congress-Division for Planetary Sciences Joint Meeting, 2011, #624.

French, R.G., Nicholson, P.D., Porco, C.C., Marouf, E.A., 1991. In: Bergstralh, J.T., Miner, E.D., Matthews, M.S. (Eds.), Dynamics and Structure of the Uranian Rings, Uranus. University of Arizona Press, Tucson, AZ, pp. 27–409.

French, R.G., Marouf, E.A., Rappaport, N.J., McGhee, C.A., 2010. Occultation observations of Saturn's B ring and Cassini Division. Astron. J. 139, 1649–1667.

Goldreich, P., Tremaine, S.D., 1978. The formation of the Cassini Division in Saturn's rings. Icarus 34, 240–253.

Goldreich, P., Tremaine, S.D., 1979. The excitation of density waves at the Lindblad and corotation resonances by an external potential. Astrophys. J. 233, 857–871.

Hahn, J.M., Spitale, J.N., 2012. Results from N-body simulations of the outer edge of Saturn's B ring. In: AAS/Division for Planetary Sciences Meeting. Abstracts 44, #513.03.

Hahn, J.M., Spitale, J.N., 2013. An N-body Integrator for Gravitating Planetary Rings, and the Outer Edge of Saturn's B Ring. ArXiv e-prints arXiv:1306.1135.

Hahn, J.M., Spitale, J.N., Porco, C.C., 2009. Dynamics of the sharp edges of broad planetary rings. Astrophys. J. 699, 686–710.

Harper, D., Taylor, D.B., 1993. The orbits of the major satellites of Saturn. Astron. Astrophys. 268, 326–349.

Hedman, M.M. et al., 2010a. The architecture of the Cassini Division. Astron. J. 139, 228–251.

Hedman, M.M. et al., 2010b. Aegaeon (Saturn LIII), a G-ring object. Icarus 207, 433–447.

Hedman, M.M., Burns, J.A., Hamilton, D.P., Showalter, M.R., 2013. Of horseshoes and heliotropes: Dynamics of dust in the Encke Gap. Icarus 223, 252–276.

Hubbard, W.B. et al., 1993. The occultation of 28 SGR by Saturn–Saturn pole position and astrometry. Icarus 103, 215–234.

Jacobson, R.A., 2003. Am Astronautical Soc. Paper 03-198, 13th AAS/AIAA Space Flight Mechanics Meeting, Ponce, PR.

Jacobson, R.A. et al., 2006. The gravity field of the saturnian system from satellite observations and spacecraft tracking data. Astron. J. 132, 2520–2526.

Jerousek, R.G., Colwell, J.E., Esposito, L.W., 2011. Morphology and variability of the Titan ringlet and Huygens ringlet edges. Icarus 216, 280–291.

Lane, A.L. et al., 1982. Photopolarimetry from Voyager 2 – Preliminary results on Saturn, Titan, and the rings. Science 215, 537–543.

Lissauer, J.J., 1985. Bending waves and the structure of Saturn's rings. Icarus 62, 433–447.

Nicholson, P.D. et al., 2000. Saturn's rings I. Optical depth profiles from the 28 Sgr occultation. Icarus 145, 474–501.

Nicholson, P.D. et al., 2011. Noncircular features in Saturn's rings: II. The C ring. In: European Planetary Science Congress-Division for Planetary Sciences Joint Meeting, 2011, #632.

Nicholson, P.D., Cooke, M.L., Pelton, E., 1990. An absolute radius scale for Saturn's rings. Astron. J. 100, 1339–1362.

Porco, C., Danielson, G.E., Goldreich, P., Holberg, J.B., Lane, A.L., 1984. Saturn's nonaxisymmetric ring edges at $1.95R_S$ and $2.27R_S$. Icarus 60, 17–28.

Renner, S., Sicardy, B., 2006. Use of the geometric elements in numerical simulations. Celest. Mech. Dynam. Astron. 94, 237–248.

Spitale, J., Porco, C.C., 2006. Shapes and kinematics of eccentric features in Saturn's C ring and Cassini Division. Bull. Am. Astron. Soc. 38, 670.

Spitale, J.N., Porco, C.C., 2010. Detection of free unstable modes and massive bodies in Saturn's outer B ring. Astron. J. 140, 1747–1757.

Tiscareno, M.S., Hedman, M.M., Burns, J.A., Porco, C.C., Weiss, J.W., Murray, C.D., 2005. Cassini ISS Observations of the Encke and Keeler Gaps in Saturn's Rings. American Geophysical Union (Fall). Abstracts 245.

Torrey, P.A., Tiscareno, M.S., Burns, J.A., Porco, C.C., 2008. Mapping complexity: The wavy edges of the Encke and Keeler gaps in Saturn's rings. In: AAS/Division of Dynamical Astronomy Meeting 39, #15.19.

Tyler, G.L., Marouf, E.A., Simpson, R.A., Zebker, H.A., Eshleman, V.R., 1983. The microwave opacity of Saturn's rings at wavelengths of 3.6 and 13 cm from Voyager 1 radio occultation. Icarus 54, 160–188.